Magnetic Nanowires with Chemical Constraints

João Fradet

Mestrado Integrado em Engenharia Física
Departamento de Física e Astronomia
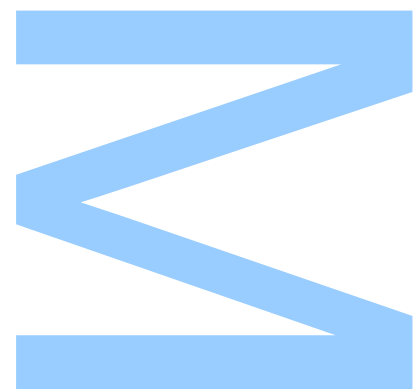2019

Orientador
Dr. João Araújo, Faculdade de Ciências

Coorientador
Dra. Mariana Proença, Faculdade de Ciências

Todas as correções determinadas

pelo júri, e só essas, foram efetuadas.

O Presidente do Júri,

Porto, _____/_____/_____

Universidade do Porto

Masters Thesis

Magnetic Nanowires with Chemical Constraints

Author:

João FRADET

Supervisor:

Dr. João Pedro ARAÚJO

Co-supervisor:

Dra. Mariana PROENÇA

A thesis submitted in fulfilment of the requirements

for the degree of MSc. Engineering Physics

at the

Faculdade de Ciências da Universidade do Porto

Departamento de Física e Astronomia

December 19, 2019

Acknowledgements

UNIVERSIDADE DO PORTO

Abstract

Faculdade de Ciências da Universidade do Porto

Departamento de Física e Astronomia

MSc. Engineering Physics

Magnetic Nanowires with Chemical Constraints

by João FRADET

Technological advancement demands constant miniaturization of functional devices. Magnetic nanostructures give promise to a vast range of applications in a wide variety of fields, from scientific research and industry to medicine and private consumption. The controlled oxidation of aluminum has provided a simple and cost effective way of fabricating metallic nanowires by nanoporous aluminum oxide template assisted electrodeposition, causing a significant boost in the study of such nanostructures.

In this thesis, nanoporous alumina templates were fabricated by anodizing aluminum. Nickel and Cobalt nanowires with non-magnetic periodic constraints were grown on anodized aluminum templates by DC electrodeposition. Structural, morphological, elementary and magnetic characterization was performed on the fabricated nanowire arrays by X-ray diffraction, scanning electron microscope, energy dispersive spectroscopy and SQUID magnetometry. The results interpreted with the assistance of micromagnetic simulations.

Different phases of the electrodepositon process were identified and correlated to the deposition of distinct structural material composition. This could provide a novel process for the control of the magnetic anisotropy of nanostructures with materials with a relevant magnetocrystalline anisotropy.

The magnetization reversal modes were studied by means of micromagnetic simulations, and interpreted in terms of characteristic length scales.

UNIVERSIDADE DO PORTO

Resumo

Faculdade de Ciências da Universidade do Porto

Departamento de Física e Astronomia

Mestrado Integrado em Engenharia Física

Nanofibras Magnéticas com Constrições Químicas

por João FRADET

O progresso tecnológico requer uma miniaturização constante de dispositivos funcionais. Nanoestruturas magnéticas compreendem um vasto número de apliações tecnologicas numa grande variedade de areas, desde a investigação científica e indústria à medicina e ao consumo particular.

O controlo da oxidação do alumínio, por anodização, permitiu um método versátil e a baixo custo de fabricação de nanofibras metálicas, por electrodeposição em moldes de óxido de alumínio, fomentando um acréscimo no estudo destas nanoestruturas.

Nesta dissertação, são fabricadas nanofibras de níquel e cobalto, por electrodeposição em corrente directa, em moldes de óxido de alumínio nanoporoso. Foram realizadas caracterizações estruturais, morfológicas, elementares e magnéticas por difracção de raios-X, microscopia electrónica de varrimento, espectrometria de dispersão de energias e por magnetometria SQUID. Diferentes fases de electrodeposição são identificadas e correlacionadas com a formação de estruturas cristalinas. Os resultados obtidos indiciam a possibilidade de controlar a anisotropia magnética de nanoestruturas de materiais de anisotropia magnetocristalina relevante, particularmente de nanofibras cilíndricas segmentadas.

Foram realizadas simulações micromagnéticas de modo a compreender o comportamento magnético de nanofibras cilíndricas, particularmente os modos de reversão da magnetização, e a nucleação e prapagação de paredes de domínio magnético. Os resultados são interpretados em termos de escalas de comprimento característico.

Contents

List of Figures

Chapter 1

Introduction

1.1 Nanotechnology

The advancement of experimental techniques in the twentieth century, such as the development of the field emission microscope in the 20s, the field ion microscope in the 50s, and the scanning tunnelling and atomic force microscopes in the 80s, permitted the study of matter at the atomic scale, thus laying the foundations for the development of nanotechnology.

Although the definition of nanotechnology has long been subject to debate, it is usually referred to as the study and manipulation of matter at the nanoscale. Nanotechnology have applications in virtually all scientific and technological fields, from medicine and biotechnology to energy production, photonics and electronics [1, 2].

The invention of the transistor was a tipping point in the field of electronics, as it permitted the amplification and switching of electric signals with low power consumption, and became the fundamental element for logic gates. Combined with the possibility of cheap mass production, it has revolutionized technology in the 20th century.

The advent of the integrated circuit (IC), in the 1960s, was a significant move towards miniaturization, as the integration of a large number of transistors into a single chip resulted in electronic circuits becoming orders of magnitude smaller, faster and more cost-effective. Gordon Moore made the observation that the number of transistors packed in an IC follows a rather predictable tendency, doubling every two years [3]. It was soon noticed a broader meaning to Moore's Law, also describing the increase in storage density of memory devices (figure 1.1).

However, as the scaling technologies reach fundamental limits, new approaches are necessary for further technological advancement. Moore himself has said he expected his famous law to die in this or the next decade, and that further miniaturization should saturate soon [5].

The physical properties of nanoscaled materials differ from their macroscopic (bulk) counterparts, as some phenomena such as surface or quantum effects become relevant or even dominant. Depending on how many dimensions are reduced to the nanoscale, nanomaterials are considered either 2D (thin films), in which the material is reduced in only one dimension, 1D (nanowires and nanotubes) in which it is reduced in the other two dimensions, or 0D where the material is reduced in all three dimensions (e. g. nanoparticles). As such, their properties and applications differ from one another.
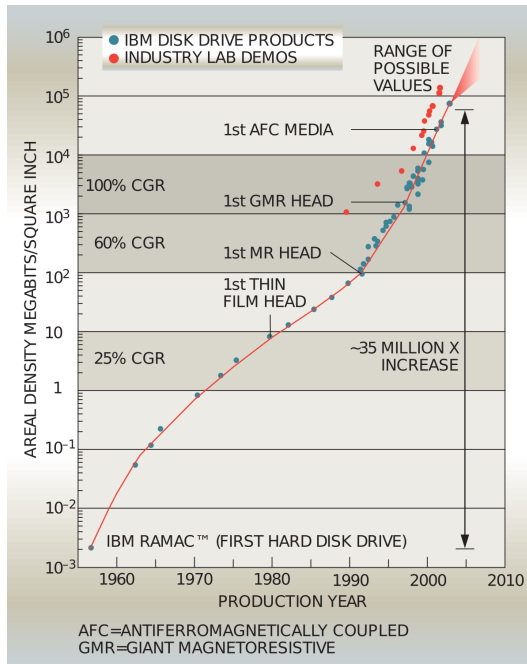
FIGURE 1.1: Hard disk drive areal density trend. Adapted from [4]

1.2   Magnetism in reduced dimensions

The magnetic properties of nanomaterials are of considerable importance in modern nanodevices. Shape plays a significant role at the nanoscale, often completely dominating other sources of the magnetic anisotropy.

The exchange anisotropy (or exchange bias) relates to the surface exchange interaction between an antiferromagnet and a ferromagnet which causes a shift of the magnetic hysteresis curve of the ferromagnet [6–8]. This effect is used for pinning the state of magnetization of ferromagnetic layers, such as the fixed layer in a spin-valve.

In nanomagnetism, it is necessary to consider a set of characteristic lengths below which, physical properties change. Most nanodevices require a magnetic material to have a single domain in at least one dimension, the maximum size a material exhibits a single domain behaviour is therefore an important characteristic length.

Another useful characteristic length is the exchange length [9], which relates to the balance between the dipolar and exchange interactions. It is of paramount importance

when considering the discretization for numerical calculations in micromagnetism and is defined as

$$l_{ex} = \sqrt{\frac{2A_{ex}}{\mu_0 M_s^2}}$$

where A_{ex} is the material exchange stiffness, μ is the vacuum magnetic permeability and M_s is the saturation magnetization.

Other characteristic lengths include the domain wall width and the coherence radius, below which nanoparticles exhibit coherent magnetization reversal. When dealing with transport properties, length scales to consider are the electrons free mean path, the elastic scattering, the spin-diffusion length and the cyclotron radius. Finally, quantum characteristic lengths need also be considered such as the Fermi wavelength for confining electrons in quantum wells and quantum dots, and the Ruderman–Kittel–Kasuya–Yosida (RKKY) interaction.

By tailoring the properties of magnetic and non-magnetic nanomaterials, one can combine them to construct more complex heterostructures to engineer functional devices.

1.3 Spintronics

The field of spintronics, in which the spin of electrons is manipulated and functionalized, has been gaining increased attention since the discovery of giant magnetoresistance (GMR) in 1988 [10, 11].

This phenomenon arises from spin-dependent scattering in ferromagnetic (FM) and conducting non-magnetic (NM) multilayers, where the electrons with their spin aligned parallel to the magnetization of the material will find less resistance than the ones with the spin aligned anti-parallel [13].

In a spin-valve [14, 15], two FM layers are separated by a NM layer. One FM layer is pinned, usually by surface exchange interaction with an anti-ferromagnetic (AF) layer [6–8], and the other remains free to switch magnetization. Considering a

FIGURE 1.2: Schematic of spin-dependent scattering in a spin-valve and two-channel model, from [12]

two-channel circuit model (one channel for each spin-current), the resistance of the spin-valve is given by

$$R_P = \frac{R_{\uparrow\uparrow}R_{\uparrow\downarrow}}{R_{\uparrow\uparrow} + R_{\uparrow\downarrow}}$$

for the state where the layers magnetization is aligned parallel to each other, and

$$R_{AP} = \frac{R_{\uparrow\uparrow} + R_{\uparrow\downarrow}}{4}$$

for when they are aligned anti-parallel to each other, where $R_{\uparrow\uparrow}$ is the resistance felt by the electrons when their spin is aligned parallel to the magnetization and $R_{\uparrow\downarrow}$ when they are aligned anti-parallel to it (figure 1.2).

This significant change in resistance permits the detection of the magnetization of the free layer by passing very small currents, having applications in magnetic biosensors [16] and in read-heads for hard-disk storage devices, permitting further scaling of such devices. A mere 8 years after the discovery of giant magnetoresistance, IBM released the first GMR product, being often regarded as an example of how quickly a fundamental scientific discovery can reach the consumer market.

The spin-valve also became the fundamental cell of the magnetic random-access memory (MRAM) [18], a non-volatile random-access memory (RAM) with relatively high bit density, where each spin-valve is used to store one bit of information (figure 1.3). The large difference in resistance permits the reading of the bits with very small currents, while the writing is performed by

FIGURE 1.3: Representation of a MRAM. Adapted from [17]

applying a localized external field by passing a current through both the bit and word lines connecting the spin-valves. The applied currents must be such that the combined magnetic fields are sufficient to switch the state of the spin-valve at the intersection of the bit and word lines, whereas not enough to do so on their own [19]. This imposes a scaling limit, as the spin valves cannot be too close such that the stray fields switch the state of neighbouring valves.

The magnetic tunnel junction [20] has a similar architecture to the spin-valve but with a thin insulator (tunneling layer) instead of the non-magnetic conducting layer. The tunneling magnetoresistance permits a further scaling of spintronic devices due to the larger change in resistance, and therefore enables the sensing of the junction state by even smaller currents. It quickly completely substituted the spin-valve in read-heads and as the fundamental cell in the MRAM. It also permits the nearly complete spin-polarization of currents flowing perpendicularly to the layers (CPP), due to the difference of tunneling probability of electrons with different spins.

The concept of spin-transfer torque (STT) [21] was first considered in the late 1970s with Berger's prediction [22] and latter observation [23, 24] that the spin of electrons would apply a torque to the domain walls causing it to move. At the time, very high currents were needed for current induced domain wall motion due to the large size of the samples. This discouraged follow-up due to the lack of practical application. With advances in nanofabrication, this concept gained increased attention due to the possibility of using smaller currents to control the magnetization and the domain wall movement, in thin films and in nanowires.

In 1996, Slonczewski [25] and Berger [26] independently showed that the magnetization of magnetic layers in FM NM multilayers could be reversed by spin polarized current flowing perpendicularly to the layers plane. This mechanism replaced the previous writing system of MRAM devices (STT-MRAM [27, 28]) due to the lower current use, permitting further scaling of the device as it diminishes the stray fields and undesired Joule heating.

1.4   Magnetic Nanowires

Magnetic nanowires are characterized by large aspect ratios and therefore, shape anisotropy plays a significant role in their magnetic behaviour, with its contribution to the magnetic anisotropy along the nanowire axis. For wires where shape anisotropy dominates and the other sources of anisotropy are negligible, the easy axis lies, therefore, along the wire axis.

If the wire is long enough, magnetic domains are formed due to magnetostatic energy minimization. The domain-walls will then be either of the head-to-head type, where the domains magnetization are pointing to each other, or of the tail-to-tail type, where they are pointing away from each other.
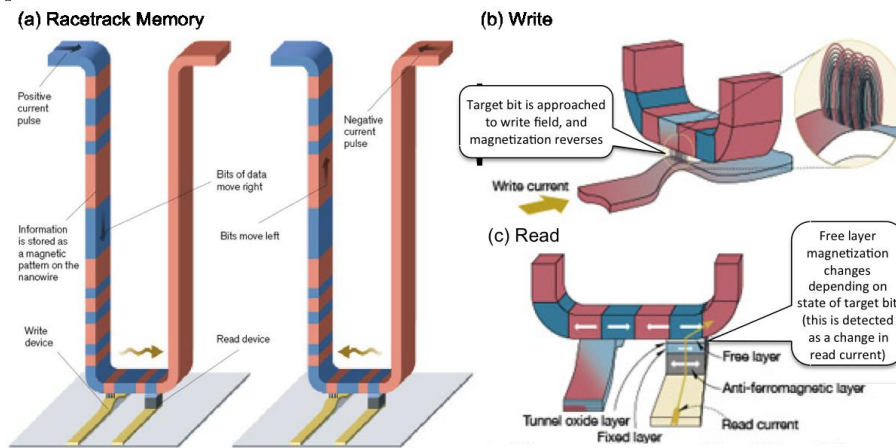
FIGURE 1.4: (a) Racetrack (b) Write head (c) Read head; Adapted from [36]

By applying a magnetic field parallel to the wire axis, these domain-walls will propagate as the field applies a torque to the magnetic moments, and the regions with the magnetization aligned parallel to the field will grow while the anti-parallel ones will shrink. The magnetic field induced DW movement then causes the head-to-head and tail-to-tail type DWs to propagate in opposite directions, and the DWs will eventually annihilate each other as the magnetization becomes saturated. An alternative way to move the DWs is by the spin-transfer torque (STT) effect, by passing a spin-polarized current through the material. Unlike with magnetic fields, the domain walls will coherently move in the same direction.

The magnetization reversal process of magnetic nanowires usually occurs by the nucleation of DWs at the wires' ends and at defects along the wire, which will then propagate, inverting the magnetization [29, 30]. The DW nucleation can be engineered to occur at sites of our choosing by fabrication constraints (defects) along the wire.

Such constraints can be either mechanical notches [31], size modulation [32] or chemical defects [33]. These constraints will also act as pinning sites where propagating domain-walls will be pinned and further energy is required to unpin them.

The precise control of magnetic domain-walls is essential for future spintronic devices like the domain-wall racetrack memory [34, 35], where magnetic bits are stored in an array of vertically aligned nanowires, and are moved by pulses of spin-polarized current to the read-write heads at the silicon substrate (figure 1.4).

This device depicts the move towards innately three-dimensional devices [37], an idea that is gaining attention due to present technologies approaching fundamental limits.

1.5   Micromagnetic simulations

Increasing computing power has permitted the study of micromagnetics by computer simulations. Several projects exist today for the development of micromagnetic simulation software, like OOMMF (Object Oriented MicroMagnetic Framework) or the GPU-based MuMax project [38].

Micromagnetic simulations are based on solving the Landau-Lifshitz-Gilbert equation which describes the magnetization dynamics:

$$\frac{d\mathbf{M}}{dt} = -\gamma \mathbf{M} \times \mathbf{H_{eff}} - \lambda \mathbf{M} \times (\mathbf{M} \times \mathbf{H_{eff}})$$

where γ is the gyromagnetic ratio, and $\lambda = \alpha \frac{\gamma}{M_s}$, where α is the Landau damping factor.

The dynamics of the magnetization reversal in cylindrical nanowires are subject of extensive study by means of micromagnetic simulations [39].

The magnetic reversal modes in nanowires occurs by nucleation and subsequent propagation of domain walls (DW) that are either transverse (TDW) or vortex type (VDW) , depending on the wire thickness. [30]. Hertel showed by micromagnetic simulations that in a nickel cone-shaped nanowire, with a diameter of 60 nm in one end and 30 nm in the other, a VDW nucleates first at the thicker end of the wire. The DW then propagates until reaching some critical thickness where it turns in a TDW. The reversal dynamics occurs by one of these DW types, depending on the nanowire thickness.

The pinning and depinning mechanisms of DWs in topological [32, 40] and chemical [33] constraints along the wire, is an active filed of study due to its promising applications in spintronic devices [34].

1.6   Thesis Outline

The objective of this thesis is the fabrication of nickel and cobalt cylindrical nanowires with periodic non-magnetic chemical constraints by electrodeposition on nanoporous alumina templates, and characterization of the fabricated nanowires. A complementary micromagnetic study was performed using the GPU accelerated MuMax3 software.

In Chapter 2, the nanowire fabrication methods are discussed, from the anodization of aluminum for the fabrication of nanoporus alumina templates to the electrodeposition

methods employed for the fabrication of samples for this thesis, as well as the experimental techniques used for their structural, morphological and magnetic characterization.

Chapters 3 and 4 discuss the details of the electrodeposition process and the experimental results for the magnetic measurements by a Superconducting Quantum Interference Device (SQUID), structural characterization by X-Ray Diffraction (XRD), and morphological and chemical composition by scanning electron microscopy (SEM) and Energy Dispersive Spectroscopy (EDS), for nickel and cobalt nanowires with non-magnetic constraints, respectively, as well as results of micromagnetic simulations.

Finally, in Chapter 5, the conclusions reached in this thesis are stated and further studies on the subject are called for.

Chapter 2

Experimental Methods

In this chapter, the experimental methods employed in this work are outlined and discussed. Section 2.1 discusses the nanowire fabrication process with particular focus on the fabrication of nanoporous alumina templates and DC electrodeposition for the gorwth of nanowire arrays. In section 2.2, a brief introduction of the characterization techniques employed in this work is given.

2.1 Nanowire fabrication

Magnetic nanowires were grown by electrodeposition on porous alumina (aluminum oxide) templates [41]. Figure 2.1 shows a schematic of the steps in the fabrication process, from a high purity aluminum foil, to the electrodeposition process in the nanoporous alumina membrane.

Squares of roughly 1,5 cm side length of a 99,999 % pure aluminum foil were cut. Prior to the anodization process, the aluminum foils were cleaned in an ultrasound bath
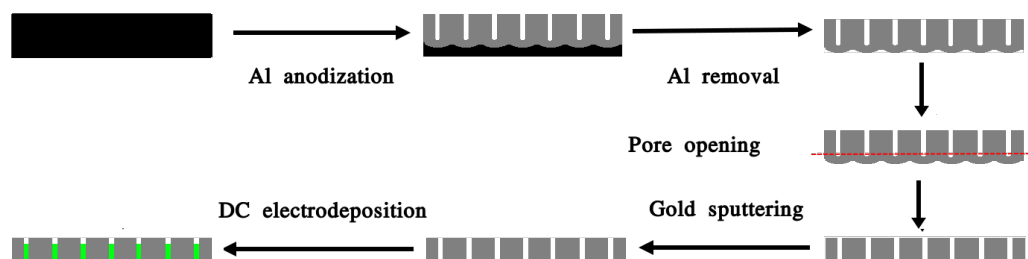
FIGURE 2.1: Schematics of the nanowire fabrication process.

for 3 minutes in acetone followed by 3 minutes in 99,9 % pure ethanol, and subsequent electropolished in order to remove any undesired material at the surface.

2.1.1 Electropolishing

Electropolishing is an electrochemical process used for the removal of undesired material, such as contaminations or an oxide layer, and to reduce the surface roughness of metals [42]. The work-piece is immersed in a typically acidic electrolyte, serving as the anode, and an electric potential is applied. The electric field lines concentrate at the top points of surface irregularities, dissolving them faster then the bottom points. This phenomenon is referred to as anodic-levelling.

The electropolishing was performed with a solution of 1/4 perchloric acid 60% ($HClO_4$) and 3/4 ethanol 99,9% (C_2H_5OH) in volume. A 20 V electric potential was applied between the aluminum foil and a platinum mesh for two minutes. This solution is highly unstable and potentially explosive, consequently the temperature needed to be kept below 10 º Celsius, by performing the electrpolishing in a bath of water and ice in equilibrium and monitoring the temperature of the electrolyte.

2.1.2 Anodization of aluminum

Nanoporous alumina templates are fabricated by the anodizating aluminum, an electric field assisted oxidation process.

Originally developed in the 1920s [43] to protect metals against corrosion by forming a protective oxide layer, some metals, such as aluminum, can form a nanoporous structure when anodized. The porous structure of aluminum oxide has since been used to make inorganic membranes [44], as well as for aesthetic pursues. Then, in the 1990s, Masuda achieved an almost perfect hexagonal organization of the pores by employing a two-step anodization technique [45]. This has sparked an enormous interest in nanotechnology [46], particularly due to its use as a template for electrodeposition of nanowires and nanotubes [41].

Aluminum is known for its high affinity for oxygen. The formation of an aluminum oxide layer at the surface of aluminum when exposed to the air is therefore, an almost spontaneous process. The applied electric field causes the oxygen ions to migrate through the insulating alumina layer, further oxidizing the aluminum, increasing the alumina layer up to some thickness determined by the applied potential.
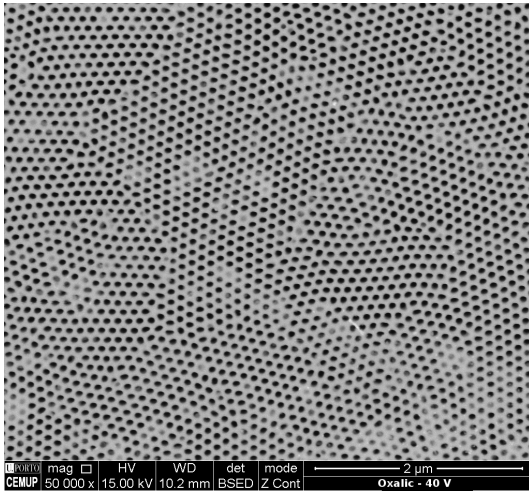
FIGURE 2.2: Top view of a nanoporous alumina template.

For a porous alumina layer to form, certain conditions have to be met [47]. These conditions will determine the pores diameter d, and the inter-pore distance d_{int}.

During the oxidation process, the aluminum undergoes a significant volume expansion. This causes a mechanical stress that leads to irregularities in the alumina layer [48]. The electric field lines will then concentrate at the bottom of these irregularities, where the thickness of the alumina barrier is lower and therefore has lower resistance (figure 2.4a). This results in a local rise of temperature which lowers the pH, dissolving the alumina at these points as the migration of oxygen keeps oxidizing the aluminum at the metal/oxide interface (m/o). The process then reaches a steady state where the rate of field-enhanced oxide dissolution at the electrolyte/metal (e/m) interface equals the rate of oxide formation at the m/o interface, keeping the barrier thickness and the pore growth speed constant. The anodization time will then determine the pores' depth.

Figure 2.3 shows a typical behaviour of the current density of an anodization process and it's four main phases. Phase I is characterized by a steep drop in the current density which corresponds to the formation of the insulating alumina barrier. When the current reaches a minimum, the barrier is at its maximum thickness. Phase II, corresponds to the pore nucleation process, the oxide barrier is thinner at the bottom of the
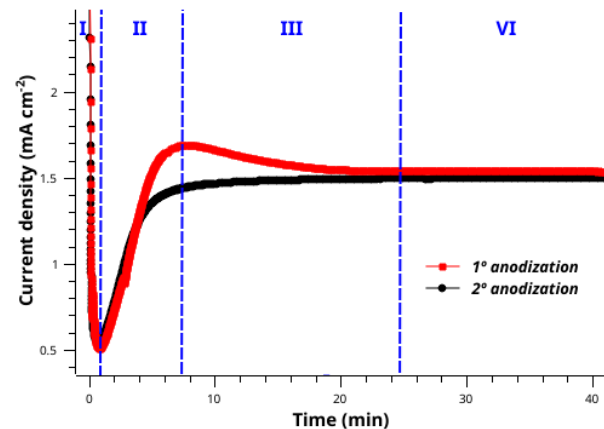
FIGURE 2.3: First and second andization curves.

pores which become low resistance channels increasing the current passing through the barrier. At this stage, the pores are disorganized and of various shapes and sizes. As the anodization continues, a self-organization process ensues as smaller pores are absorbed

by larger ones, leading to a slight decrease of current and the bottom becomes increasingly more organized (phase III). Eventually, this process stabilizes and a highly ordered hexagonal structure is formed at m/o interface as the pore growth continues.

Two-step anodization process   Due to the highly organized structure of the aluminum surface at the bottom of the pores Masuda [45] found that by performing a second anodization after chemically etching the porous alumina layer, one could grow pores with a nearly perfect honeycomb hexagonal structure (figure 2.4).

The highly organized hexagonal structure that remains at the aluminum surface acts as the pores' nucleation sites, which will then grow with a highly organized manner. It is then expected the absence of the decrease in current density in phase III during the second anodization, as can be observed in figure 2.3. Figure 2.2 shows a scanning electron microscope (SEM) top view of a alumina template fabricated in this work. It shows the pores' highly organized hexagonal structure. It can also be seen a grain structure, where the hexagonal meshes are not aligned. This limitation can be overcame by nanoimprinting in the "right places" the aluminum prior to anodization [45, 49]

FIGURE 2.4: Schematics of the two-step anodization process: a) The field lines concentrate at the bottom of the oxide layer's irregularities; b) 1st anodization c) Alumina is removed, leaving a highly organized pattern; d) 2_{nd} anodization

2.1.2.1   Anodization details

The nanoporous alumina templates were fabricated by a two-step anodization process. The first anodization was performed at 40 V on an aqueous solution of 0,5M Oxalic acid ($H_2C_2O_4$) for 24 hours and temperatures between 2° and 6 ^{o} Celsius, resulting in a pore diameter of roughly 30 nm and an inter-pore distance of 105 nm. A platinum mesh was used as the cathode. The alumina was then removed by a solution of 0,4 M phosphoric acid (H_2PO_4) and 0,2 M chromic acid (H_2CrO_4) for 24 hours at room temperature. Alternatively, at 40 ^{o}C, the time can be reduced in half. The second anodization was performed for 48 hours under the same conditions, resulting in a membrane thickness

of about 120 μm. This longer anodization results in a thicker membrane which permits the fabrication of longer nanowires. A thicker template also means it is easier to handle without breaking.

2.1.3 Aluminum removal and pore opening

The remaining aluminum was then removed by wet chemical etching in a 0.2M CuCl$_2$ and 4.1 M HCl aqueous solution. The alumina barrier at the bottom of the pores was then removed by floating the membranes in a 10 % diluted phosphoric acid solution at room temperature. As soon as the membranes sink, meaning the pores bottom are open, they are immediately rinsed in water. This process can be accelerated by increasing the temperature. Because the etching is not a perfectly homogeneous process, some pores will be opened sooner than others, and the acid will flow up the pores, this results in a non-uniform pore widening. Posterior SEM visualization determined that, after this process, the pore diameter was around 50 nm, ranging from slightly over 30 nm to about 60 nm (figure 2.2).

2.1.4 Sputtering

To serve as the working electrode for the electrodeposition, a gold film is sputtered at the bottom of the alumina membranes. This was performed with a bench-top ScanCoat Six sputter from HHV.

Sputtering is a widely used technique in industry as both a physical deposition technique and for etching material due to its versatility and the high
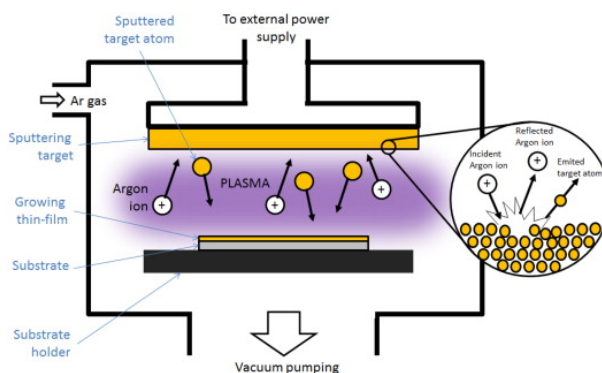
FIGURE 2.5: Schematics of the sputtering process. Adapted from [50]

quality of the deposited thin films. It consists in the deposition of a material, usually metals, by momentum transfer. An inert gas is introduced in the chamber and a voltage is applied between the target (cathode) and anode (figure 2.5). The target is the material which is deposited and the substrate is usually placed over the anode.

The free electrons are accelerated and collide with the Ar atoms. These are ionized and second electrons are released, which in turn will ionize another atoms leading to a gas breakdown, thus sustaining the plasma.

The Ar^+ ions are accelerated towards the (gold) target, sputtering its atoms. These will then condense onto the substrate, resulting in a high quality thin film.

2.1.5 DC Electrodeposition

The electrodeposition was performed with a potentiostat in a three electrode cell, with a Ag/AgCl reference electrode from Metrohm and a platinum mesh counter electrode.

Also referred to as electroplating, it has long been used in industry for growing films due to its cost effectiveness and its wide range of applications. It consists in the reduction of metal ions in an electrolyte by applying an electric potential. More recently, it has become a rather cheap method for the fabrication of nanostructures.

The electrodeposition on nanostructured templates, such as nanoporous alumina for nanowire growth, has been under continuous study [36].

The crystalline structure of certain magnetic materials such as cobalt is relevant for the anisotropic behaviour, often dominating other sources of magnetic anisotropy such as shape. It then becomes important to control the crystalline structure of these materials. By manipulating the electrodeposition conditions, such as the electrolyte pH, the applied potential, the substrate on which the material is grown and the deposition time, one can control the preferential crystal growth direction and, as a consequence, the magnetic anisotropy [51–54]. The electrodeposition under an applied magnetic field is also subject to study [55].

The applied potential in a three electrode DC electrodeposition cell is such that the electric potential at the sample (working electrode) is constant with respect to the reference.

Prior to the electrodeposition of the magnetic nanowires, gold was electrodeposited with a commercial electrolyte suloution (Orosene E +4 g/lt from Italgalvano s.p.a.) at -1 V for 5 minutes to improve the electrical contact.

Single-bath method   When fabricating multilayered thin films or segmented nanowires, one could simply change the electrolyte for every layer deposited. However, this is a rather tedious and time consuming process, and not very attractive for industrial use.

The single-bath method is a technique that permits the alternated deposition of different elements using the same electrolyte by modulating the applied potential.

Taking nickel and copper as an example: Copper reduces at -0,4 V. At -1 V, both nickel and copper are reduced and an alloy is deposited. Low concentrations of copper ensure low contamination in the nickel segments, at the cost of deposition time as the copper segments will grow slower.

A significant limitation of this method is that only specific combinations of ionic species can be deposited. More complex electrodeposition cells have been developed for the automation of dual-bath electrodeposition techniques [56, 57].

Further electrodeposition details are presented in Chapters 3 and 4 for the specific materials deposited.

2.2   Characterization techniques

2.2.1   Scanning Electron Microscopy (SEM) and Energy Dispersive Spectroscopy (EDS)

The SEM / EDS exam was performed using a High resolution (Schottky) Environmental Scanning Electron Microscope with X-Ray Microanalysis and Electron Backscattered Diffraction analysis: Quanta 400 FEG ESEM / EDAX Genesis X4M.

Scanning electron microscopy permits the visualization of materials at the nanoscale, giving information regarding its morphology and chemical composition (atomic number).

Even though the first commercial model of a scanning electron microscope was introduced in 1965, the concept of scanning electron microscopy dates from the 1930s, roughly around the same time as the transmission electron microscope (TEM).

The principle of electronic microscopy is in the employment of an electron beam in order to produce images of samples of various materials. An accelerated electron beam, whose ondulatory behaviour is associated with a De Broglie wavelength which decreases with the kinetic energy, reaches sub nanometre values in normal electronic spectroscopy conditions. This permits the realization of electron beams with very small cross-section diameter and aperture, achieving a far superior resolution and depth of field than it is possible in optical microscopy. A series of electric and magnetic fields act as the optical system to focus and deflect the beam to scan the sample surface.
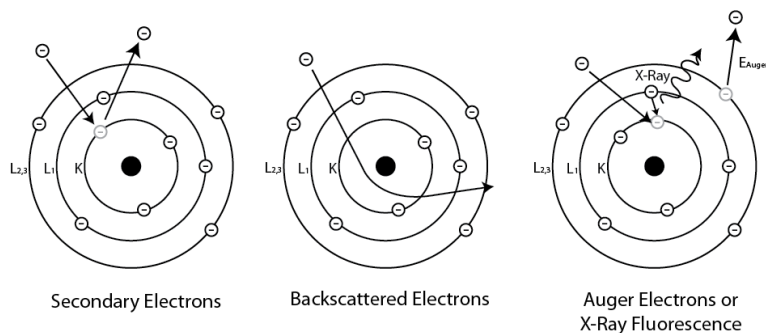
FIGURE 2.6: Elastic and inelastic interactions. Adapted from [58]
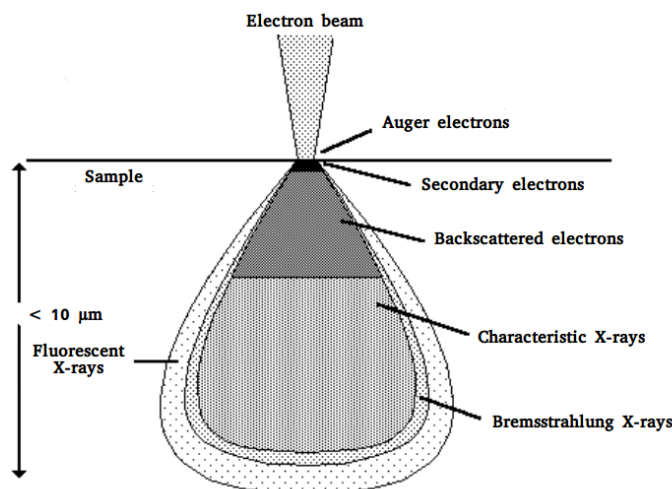
FIGURE 2.7: Relative volume of radiation emission. Adapted from [59]

The sample surface is scanned by the electron beam (primary electrons), which inter-acts with the sample material.

Figure 2.6 shows a schematic of the different (elastic and inelastic) interactions occur-ring at the sample. These interactions can be elastic, where the resulting electrons are of the same energy as the incident ones (primary electrons), or inelastic where the interac-tion results in an energy loss. By means of these interactions, the sample emits radiation such as secondary electrons, backscattered electrons and X-rays, each carrying distinct information of the morphology, and chemical composition, forming an image, as it is the case for the emitted electrons, or an X-ray spectrum.

Alternatively, the primary electrons can instead be absorbed by the sample, creating a charge accumulation that produce image instability and high contrast effects due to local electric fields interacting with the emitted electrons. It is then necessary to ensure conductive paths from the sample surface to the mass, if the surface is not conductive itself.

Secondary electrons   The secondary electrons (SE) result from inelastic interactions where the electrons in the sample atoms are knocked off their orbital by the primary electrons or by backscattered electrons. Owing to their low energy, the emitted SE originate from the point of incidence of the beam and its immediate vicinity (figure 2.7), while the ones that originate from interactions occurring deeper in the material are diffused before they reach the surface. This signifies that a SE image contains mostly information about the surface of the material.
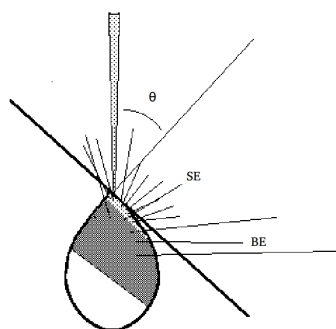
FIGURE 2.8: Topographical effect in SE and BE emission. Adapted from [59]

The intensity of the emitted secondary electrons is strongly dependent on the angle of incidence with its highest values at grazing incidences, as it is schematized in figure 2.8. This results in an image with a strong topological contrast, similar to a photography. The emission of SE varies irregularly with the chemical composition. The contrast originating from chemical variations results from interactions with backscattered electrons, whose intensity depends on the atomic number of the material, and it is only observable on low topography, and significant difference in atomic number.

Backscattered electrons   Backscattered electrons (BE) result from the deflection of the primary electrons by the material atoms nucleus. These are usually elastic or quasi-elastic interactions with no or very low energy loss.This signifies that the BE from greater depths reach the surface and are emitted. The resolution of the resulting image is therefore fundamentally dependent of the incident beam energy, and the resolving power is significantly less than with SE.

Perhaps the most important aspect of BE is that backscattering rate increases with the atomic number, carrying information on the chemical composition of the material.

Like the secondary electrons, the intensity of the backscattered electrons increases with the angle of incidence (figure 2.8), however the BE emission is highly directional. The intensity is therefore dependent on the location of incidence relative to the detector.

X-rays and Energy Dispersive Spectroscopy (EDS)   There are two distinct sources of X-rays in electron spectroscopy, one is a continuous spectrum that results from the interaction of electrons with the electric field from the material nucleus (Bremsstralung). The

other results from the vacancies left by the creation of secondary electrons that are readily occupied by electrons from higher energy orbitals. Energy conservation is assured by either the emission of an electron from a higher energy orbital (Auger electron), or by the emission of an X-ray photon.

The emitted X-rays have therefore, characteristic wavelengths that permit the determination of the chemical composition. This is the basis of Energy Dispersive Spectroscopy.

2.2.2   X-Ray Diffraction (XRD)

The structural characterization for this work was performed with a SmartLab, Automated multipurpose X-ray diffractometer from Rigaku.

X-ray diffraction is a characterization technique that permits the identification of the crystalline structure of materials.

X-rays have the wavelength of the same order of crystallographic cells (about 1 Å) The incident X-rays interfere with the electron orbitals of the atoms and are diffracted at different crystallographic planes which will then interfere either constructively or destructively, creating a diffraction pattern read by the detector, which results in intensity peaks at characteristic angles of the crystallographic structure.
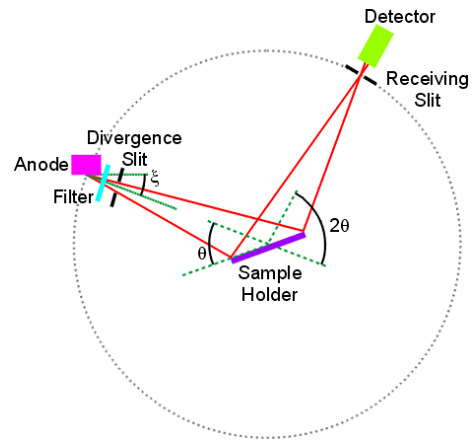
FIGURE 2.9: Bragg-Brentano geometry. Adapted from [60]

The relationship between the spacing of the crystallographic planes and the angle of diffraction is given by Bragg's law:

$$n\lambda = 2d_{hkl}sin(\theta)$$

where n is a natural number resulting from the waves periodicity, λ is the X-ray wavelength, θ is the angle of incidence and d is the inter-planar distance of miller indices hkl.

The broadening of the diffraction peaks gives the average size of the ordered crystalline grains by Scherrer's equation:

$$\tau = k\frac{\lambda}{\beta cos(\theta)}$$

where β is the peak width at the centre of intensity, and k is the dimensionless shape factor, with a value close to unity.

An X-ray diffraction machine can work in several geometries:

Bragg-Brentano geometry   This geometry is useful for $\theta\,2\theta$ measurements as it focuses the diffracted beam at the detector, allowing for increased intensity.

This requires the X-ray source and the detector to be placed at the same distance from the sample, creating a spherical surface where the diffracted beam is focused.In $\theta\,2\theta$ measurements, the angle of the incident X-ray beam is equal to the angle of detection, as the movement of the X-ray emitter accompanies the movement of the detector to scan diffraction pattern. The θ refers to the angle of incidence, while the 2θ refers to the detector angle with respect to the incident beam (figure 2.9).

The X-ray penetration in the sample depends on the angle of incidence. This results in the deeper probing of the sample as the angle increases.
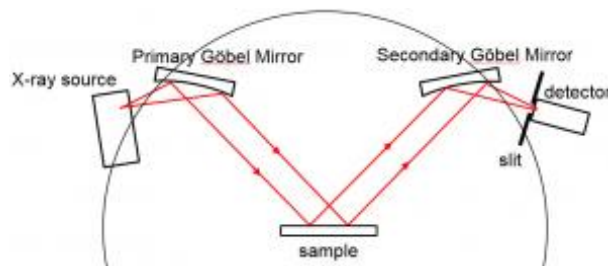
FIGURE 2.10: Parallel beam geometry. Adapted from [61]

Parallel beam geometry   The parallel beam geometry is useful for grazing incidence measurements with a fixed angle of incidence ($\omega\,2\theta$). The emitted divergent X-ray beam is reflected on a Goebel mirror which collimates the beam that is then incident on the sample. The diffracted beam is again reflected in a Goebel mirror and is focused at the detector (figure 2.10).

In a ($\omega\,2\theta$) measurement, the incident beam is fixed at an angle ω and the diffraction pattern is scanned by the detector scans.

By performing several measurements at different ωs, the structural properties of the samples at different depths can be measured.

2.2.3   Superconducting Quantum Interference Device (SQUID)

The magnetic measurements were performed with a Quantum Design/EverCool Superconducting Quantum Interference Device (SQUID) magnometer.

The SQUID is essentially a magnetic flux to voltage converter consisting in a superconducting loop with Josephson junctions. The signal from the pick up coils induces a

current in the SQUID. The resulting voltage constitutes the output signal resulting in a highly sensitive magnometer.

In this work, only M(H) measurements were performed at 300 K.

Chapter 3

Nickel Nanowires with Chemical Constraints

In this chapter, the fabrication and characterization of nickel nanowires are discussed and the results interpretation is assisted by micromagnetic simulations.

In section 3.1, a general study of nickel nanowires magnetic behaviour is performed by means of micromagnetic simulations as a basis for the interpretation of more specific simulations and experimental results. Section 3.2, discusses the details of the electrodeposition process of Ni/Cu segmented nanowires. In sections 3.3, 3.4 and 3.5, morphological, elementary, structural and magnetic characterization results are discussed. Finally, section 3.6, finalizes the chapter by stating the conclusions of the study on nickel nanowires.

3.1   Micromagetic Simulations

In order to get a better understanding of the magnetic behaviour of nickel nanowires, micromagnetic simulations were performed using the MuMax3 software, which uses the finite difference method, dividing space into a parallelepipedal mesh. This inevitably results in an error associated with the staircase discretization of a cylindrical geometry of the nanowires.

The common simulation parameters for nickel were used: a saturation magnetization of $490 \times 10^3 \, A \, m^{-1}$, and an exchange constant of $9 \times 10^{-12} \, J \, m^{-1}$. A Landau damping factor of $0,5$ was assumed in order to ensure rapid convergence. The nickel wires were considered pure. It was checked that the introduction of the magnetocrystalline anisotropy gave only negligible differences in the results, for any direction.
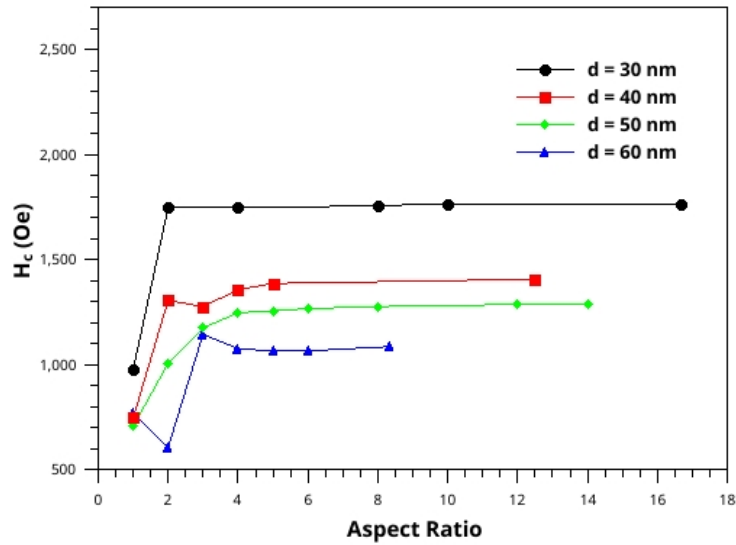
FIGURE 3.1: Coercivity versus the aspect ratio (length/diameter) for various wire diameter.

The simulated space was a parallelepipedal mesh with unit cell size of 5 nm in the wire axis which is smaller than the nickel exchange length $l_{ex} = 7,72\,nm$.
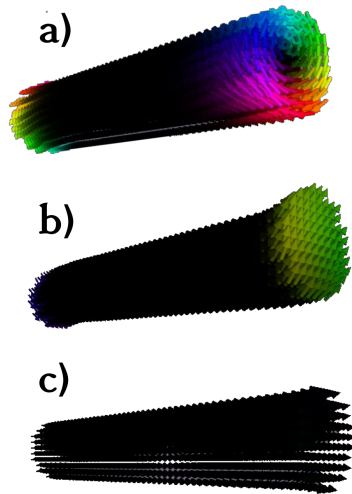
FIGURE 3.2: DW nucleation process; a) Nucleation of a VDW in a 60 nm diameter nanowire ; b) Nucleation of TDW in a 50 nm diameter nanowire; c) No nucleation occurs in a 30 nm diameter nanowire, magnetiation reversal occurs by coherent rotation.

In the perpendicular cross-section plane, it was varied such that the wire had 20 cells along its diameter in order to better simulate a cylindrical geometry.

The hysteresis of single wires with varying lengths and diameters, with the field applied parallel to the wires, was simulated.

Figure 3.1 shows the coercivity of the wires versus their aspect ratio (length/diameter), for different diameters. It shows that, as a general rule, the coercivity increases with the wire length until it reaches aspect ratio of about 5, where the coercivity remains constant and the wire essentially behaves as if it were infinite.

The magnetization reversal of nickel nanowires occurs essentially by three distinct means, depending on their diameter (figure 3.2). For wires with a diameter of 60 nm, the reversal occurs by nucleation and propagation of a vortex domain wall (VDW). For wires from 55 nm to 40 nm diameters, the system cannot maintain a VDW and the reversal occurs by nucleation

and propagation of a transversal domain wall (TDW). It should be noted that it is not a pure TDW as the magnetic moments at the cross-section at the centre of the DW are not perfectly aligned. For simplicity, in this work, it will be referred to as a TDW instead of quasi-TDW. Finally, for wires with 30 nm and 35 nm diameter, the wire size is below some mono-domain limit and therefore cannot sustain a domain wall and the magnetization reversal only occurs when the magnetic field is high enough to switch the magnetization by coherent rotation (CR). The value of the coercivity is consistent with analytical calculations based on the Stoner–Wohlfarth model for the coercivity of coherent rotation for nickel nanowires with 30 nm diameter [62]. The conflict with experimental results in [62], which suggests that, for 30 nm diameter nanowires, the magnetization reversal occurs by the propagation of a TDW, may be due to the dipolar interactions of a large number of vertically aligned nanowires in the measured sample.

An exception exists for the case of a 60 nm diameter wire with aspect ratio 1. Although the diameter tends to nucleate a VDW, the wire length is shorter that the VDW width and therefore, has a distinct magnetic behaviour. Instead of having a magnetization reversal by DW nucleation and propagation, when a certain field is reached H_v and saturation can no longer be maintained , the outer magnetic moments (shell) will adopt a vortex state slightly tilted towards the core while it remains saturated. As the field increases, the vortex shell will rotate (maintaining its chirality) away from the saturated core and towards the direction of the applied magnetic field, until the switching field H_s is reached when the core is switched and the wire is again saturated in the reversed state.

For an infinite wire ($l = 500\,nm$), the coercivity decreases with the wire diameter in an almost linear fashion, as can be seen in figure 3.3.

In order to study the influence of a non-magnetic segment in a nickel nanowire, two coaxial wires of 50 nm in diameter and 100 nm in length, separated by some distance δ, were simulated. If the wires are far enough, they will behave independently, and in the case where $\delta = 0$, the wires become a
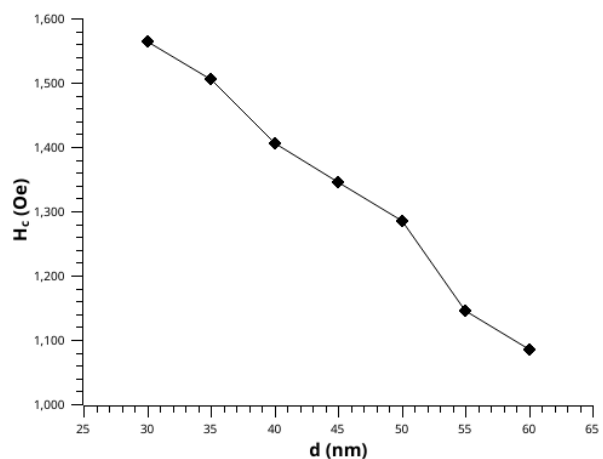
FIGURE 3.3: Nanowire coercivity with respect to diameter.

single wire of length 200 nm. The unit cell size in the wire axis direction was reduced as the spacing δ demanded. Figure 3.4 shows an exponential increase of the coercivity as de distance δ shortens, and that for spacer widths grater than $60nm$, the wires behave independently.
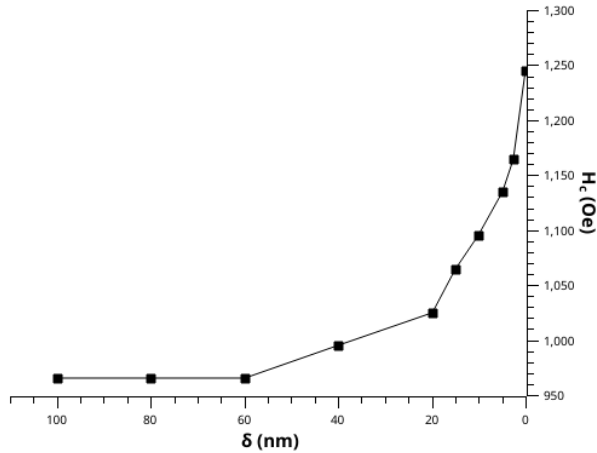
FIGURE 3.4: Coercivity of two nanowires in the same symmetry axis separated by a distance δ.

The DW nucleation occurs at the extremities of the segments, and therefore, at the NM constrictions and at the nanowire ends. Due to the dipolar interactions at the constriction forcing the magnetization to stay in place, the DWs nucleated at the nanowire ends unpin at lower magnetic fields, propagating through the wire and reaching the NM constriction. At this point the dipolar field at the constriction now forces the reversal of the next FM segment and the DW propagates through the constriction without the need to further increase the magnetic field. In other words, the magnetization reversal occurs only by the propagation of the DWs nucleated at the nanowire ends and not at the NM constrictions.

Up until now, the term infinite has been used to refer to a nanowire long enough so that its coercivity no longer changes by differences in length, conserving, however, the discontinuity at the nanowire ends where the DW nucleation occurs.

In order to simulate an infinite nanowire without the discontinuity in the nanowire ends, the magnetic surface charges were removed, by introducing the appropriate boundary conditions, eliminating the discontinuity of the magnetization. A spacer was placed

FIGURE 3.5: Coercivity of infinite nanowires with spacer δ. For $\delta = 40$ nm and larger, the magnetization reversal occurs by DW propagation (DWP). For shorter spacings, the reversal occurs by coherent rotation (CR).

at the middle of the nanowire so that if the magnetization reversal occurs by DW prop-
agation the DWs will be forced to occur at the spacer. Figure 3.5 shows the coercivity of
such an infinite wire with 50 nm in diameter and spacer varying widths.

It is found that, for spacer widths of 20 nm or less, the dipolar interactions prevent the
nucleation of DWs and the magnetization reversal can only occur by coherent rotation,
resulting in a significant increase in coercivity.

3.2 DC Electrodeposition of Ni/Cu segmented nanowire arrays

The reduction potentials of nickel and copper are sufficiently apart in order for the single-
bath method to be employed. An electrolyte of $0.5M\,NiSO_4 \cdot 7H_2O\ +\ 0.005M\,CuSO_4 \cdot$
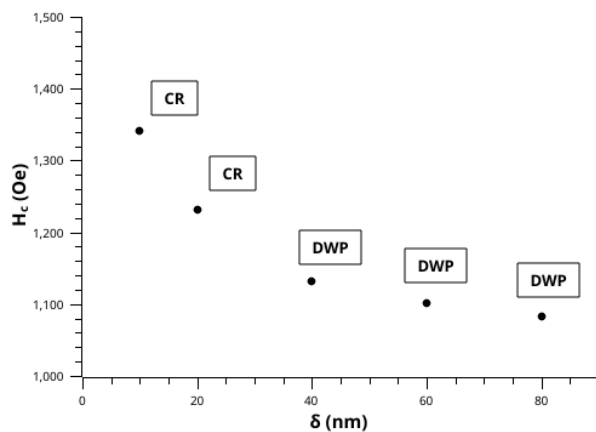$5H_2O +\ 0.6M\,H_3BO3$ was used. The boric acid acts as a buffer keeping the pH at 4 [63].
Nickel is deposited at -1 V while Copper was deposited a -0,4 V.

Non-segmented wires of nickel and copper were fabricated by electrodeposition with
the same electrolyte at -1 V and -0,4 V in order to grow nickel and copper nanowires
respectively. Energy-dispersive X-ray spectroscopy (EDS) analysis shows no nickel con-
tamination in the copper wires, as expected. More importantly, copper energy peaks were
absent in the EDS spectrum of the nickel wires, indicating a negligible copper contamina-
tion.

Three samples were fabricated with different copper segment widths. Each sample
had 15 Ni/Cu segments. Nickel was deposited for 417 s while copper was deposited for
60 s, 120 s and 180 s.

Prior to Ni/Cu segmented electroeposition, copper was deposited for three minutes
so all nickel segments are deposited over a copper substrate. Figures 3.6 and 3.7 show the
applied potential and the measured current response during the electrodeposition process
of one of the samples.

Even though the current caused by the cathodic reaction (cation reduction at the cath-
ode) is but one contribution to the overall current response, it still gives an indication of
the quantity of material being reduced. Note that the current intensity when depositing
nickel is about forty times the deposition current for copper while the applied potential
is of the same order of magnitude. This is due to the difference of concentration of the
different elements in the electrolyte. The deposition rate of copper is, therefore, much
slower than of nickel.
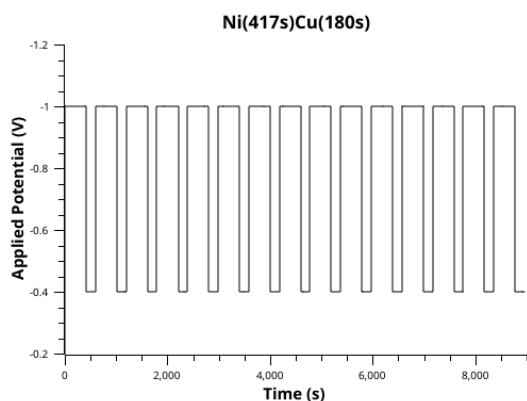
FIGURE 3.6: Applied potential with respect to the reference.
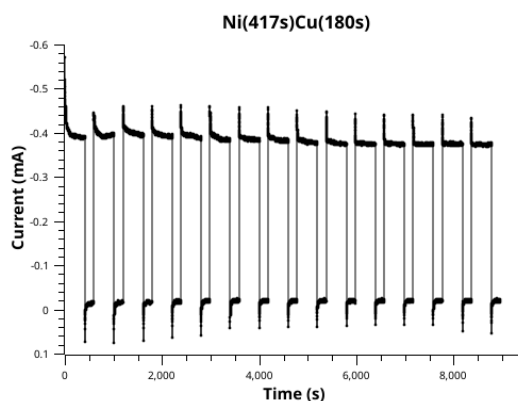
FIGURE 3.7: Current response of the electrodeposition process.

3.3   Scanning Electron Microscopy

The membranes cross-sections, exposing the nanowires, were visualized in a scanning electron microscope (SEM).

The small difference in atomic number between nickel and copper elements results in very little contrast in SEM visualization. Furthermore, backscattered electrons from nanowires behind the cross-section, whose segments are not necessarily aligned, are also emitted, effectively resulting in the impossibility of distinguishing the nanowires segments, particularly for very small copper constrictions.

It was then necessary to selectively etch the nanowires segments. The membranes cross-section were dipped in an aqueous solution of 10 % diluted nitric acid for about two seconds, dissolving the copper segments.

In figure 3.8, an example of SEM image of the cross-section of in-membrane wires is shown. The bright segments correspond to nickel while the darker ones correspond to the copper segments which were chemically removed.

The selective etching permitted the measurement of the nanowires segments, tabeled in table 3.1.
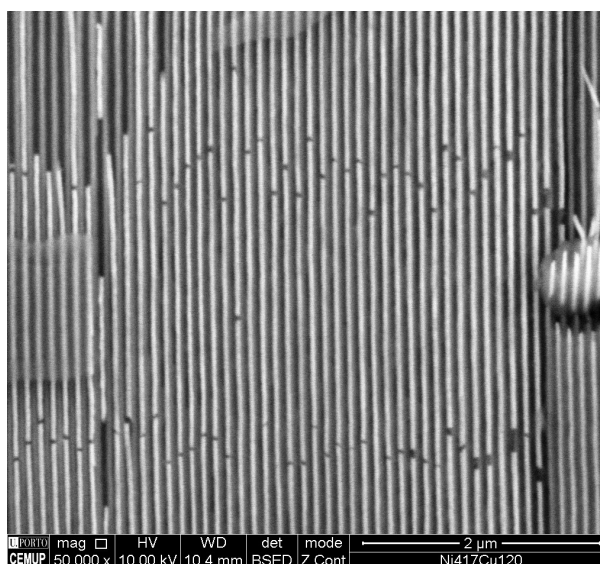
FIGURE 3.8: Cross-section SEM visualization of sample 2.

Sample	Deposition time	Segment length
1	Ni(417 s) / Cu(60 s)	Ni (2 μm ± 200 nm) / Cu (18 nm ± 5 nm)
2	Ni(417 s) / Cu(120 s)	Ni (2 μm ± 200 nm) / Cu (35 nm ± 5 nm)
3	Ni(417 s) / Cu(180 s)	Ni (2 μm ± 200 nm) / Cu (46 nm ± 5 nm)

TABLE 3.1: Deposition times and segment lengths of the Ni/Cu samples.

The Nickel segments were of about 2 μm and therefore, magnetically, should behave as infinite. The copper constraints were measured to be of 18 nm, 35 nm and 46 nm for 60 s, 120 s and 180 s long deposition respectively. The uncertainty represents both the variation of length of different segments, and the resolution of the SEM image.

3.4 Structural characterization

X-ray diffraction was performed with a Bragg-Brentano geometry and 2θ angles were scanned from 30 º to 90 º.

Figure 3.9 shows the diffraction pattern for all three nickel samples with different copper constriction widths on a logarithmic scale. Ni is shown to have a fcc cubic structure with a preferential orientation in the (220) planes.

Other peaks are also visible on a logarithmic scale. The absence of the three first peaks in sample 1 is due to fact that the sample was placed with the top side up, contrary to the others that were placed with the bottom side up. The X-rays do not probe deep enough
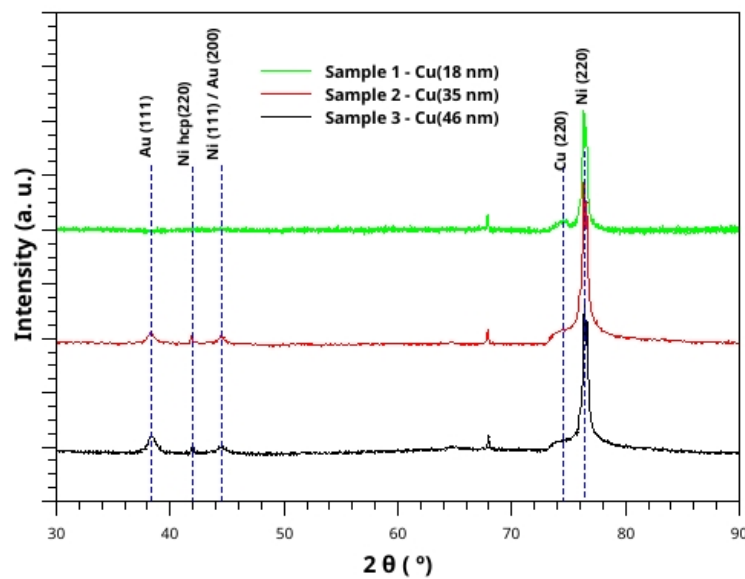
FIGURE 3.9: X-ray diffraction pattern for Ni/Cu segmented nanowires.

in the sample to detect gold contact. It is then probable that the $2\theta = 44,3°$ peak is due to gold.

A peak which can be attributed to a nickel hcp structure is visible. A meta-stable Ni-hcp phase has been reported previously, and is generally thought to be non-magnetic [64–67]. The absence of this peak in sample 1, indicates that the possible nickel hcp structure occurs only at the Ni/Cu interfaces, and Ni is deposited onto Cu. Another possibility is formation of Ni-hcp by the variation of the electric potential. When the potential is switched, a dynamic phase of the electrodeposition occurs before it reaches equilibrium, potentially forming a meta-stable at the first stages of the electrodeposition process of the Ni segments. When the first Ni segment is deposited, the potential lowers from 0 V to -1 V, therefore the step is of $\Delta V = -1\,V$, while in the other segments is $\Delta V = (-1) - (-0,4) = -0,6\,V$. It is then possible that this phase only occurs in the first Ni segment.

Both the potential step and the nickel deposition occurring on a copper segment rather than on itself can form different crystalline structures. However, more systematic study on the electrodeposition process is required for more conclusive results.

3.5   Magnetic Characterization

Magnetic characterization was performed with a SQUID magnometer. Measurements of the magnetization versus the applied field M(H) were performed at room temperature (300 K).
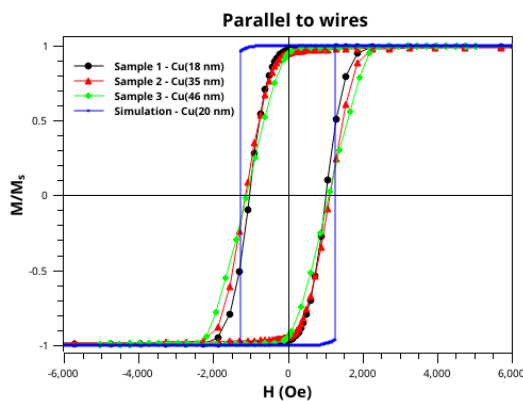
FIGURE 3.10: M(H) with field applied parallelarly to the wires.

FIGURE 3.11: M(H) with field applied perpendicularly to the wires.

Figures 3.10 and 3.11 show the hysteresis for the three fabricated samples compared to a single simulated wire, with the field applied parallel and perpendicular to the wires axis. It is clear that the magnetic easy axis is along, or close to the wires axis. This is expected since shape should play a dominant role.

All samples have similar hysteresis, as all magnetic segments are long enough to be considered as if they were infinite. And therefore, the non-magnetic segments are irrelevant.

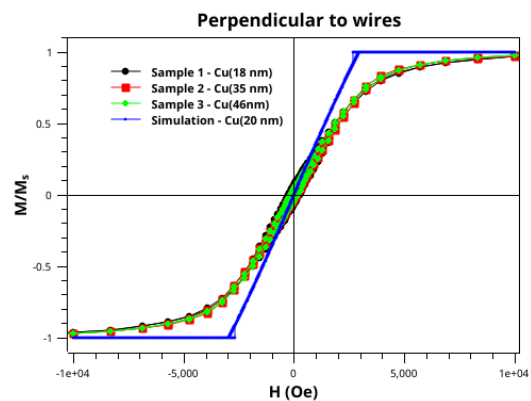The difference in squareness with respect to the simulation is due to the demagnetizing field of the large array of parallel wires in the template, as the simulation is of a single nanowire due to computational power limitations[68]. The value of coercivity is fairly consistent with the micromagnetic simulations. And comparison with analytical calculations [62] indicate a reversal process occurring by nucleation and propagation of a transversal domain wall.

Magnetic measurements at room temperature can cause some difficulties when saturating the material due to thermal oscillations on the magnetic moments, even though it is well below the Curie temperature for nickel, which is 355º C for bulk.

Much of the material in the sample is the alumina template, which has diamagnetic behaviour. Indeed, as a very broad estimate, employing Nielsch's 10 % rule [47], and assuming the pores are about a quarter filled, the percentage of the ferromagnetic material in the sample is about 2,5 % in volume, the rest being the diamagnetic template. Neglecting the areas of the alumina template where the material was not electrodeposited due to defects in the electrical contact or the areas outside the electrodeposition cell. All linear contributions were then removed by data processing.

3.6 Conclusions

Micromagnetic simulations were performed in order to study the magnetic behaviour of nickel nanowires, particularly the magnetic reversal modes, and the DW nucleation in non-magnetic spacings.

The magnetization reversal was found to occur in three distinct modes, either by nucleation and propagation of a TDW, VDW, or by coherent rotation, were all magnetic moments revert simultaneously. The mode in which the wires' magnetization revert depends essentially on the nanowires diameter. For aspect ratios larger than 5, nickel nanowires

essentially behave as if they were infinite in length (keeping the extremities where DW are nucleated).

Due to the dipolar interactions at the NM constrictions forcing the segments to keep their magnetization, the DWs nucleated at the nanowires ends will unpin at lower magnetic fields, therefore determining the reversal mode and the coercivity as the magnetization switches in a single step.

By annulling the surface charges at the nanowire ends, the DW nucleation is forced to occur at the constraints. This permitted the study of the DW nucleation at the constraints. It was found that the DW nucleation only occurs at constraints widths greater than 20 nm, for simulated nanowires with 50 nm in diameter.

Arrays of nickel nanowires with copper constraints were fabricated by DC electrodeposition on nanoporous alumina templates.

The samples were characterized by SEM, EDS, XRD and SQUID for their morphological, chemical and structural composition and for their magnetic behaviour.

The minimal contrast between nickel and copper segments on a SEM due to the small difference in atomic number causes the distinction of the segments to be virtually impossible. It was necessary to selectively etch the copper segments prior to SEM characterization.

XRD showed a fcc struture with a preferential orientation in the [110] direction. An X-ray diffraction pattern peak can be attributed to the (220) crystallographic planes of a hcp structure, possibly forming at the Ni/Cu interfaces, occurring in the first stages of electrodeposition. This could provide a way of fabricating non-magnetic structural constraints by modelating the electrodeposition potential in nickel nanowires.

The performed magnetic and morphological characterization of the fabricated nanowires are fairly in conformity with the expected from the micromagnetic simulations, since each segment, in all samples, is long enough to be considered an infinite wire.

Chapter 4

Cobalt Nanowires with Chemical Constraints

In this chapter, the fabrication and characterization of cobalt nanowires with chemical constraints are discussed.

Section 4.1 discusses the details of the electrodeposition process of segmented Co/Cu nanowires. In sections 4.2, 4.3 and 4.4, the morphological, elementary, structural and magnetic characterization results are discussed. Section 4.6 concludes the chapter by giving an overview of the conclusions.

4.1 DC electrodeposition of Co/Cu segmented nanowire arrays

The electrodeposition of segmented Co/Cu nanowires was performed employing the single-bath method since the reduction potetial of both elements is distinct enough. Cobalt was deposited at -1 V while Copper was deposited at -0,6 V, and a $0,4M\,CoSO_4 \cdot 7H_2O + 0,005M\,CuSO_4 \cdot 5H_2O + 0,4M\,H_3BO3$ electrolyte with pH = 4 was used.

Non-segmented Co and Cu were electrodeposited for the characterization of the segments chemical constitution. EDS shows no Cu contamination on Co and vice-versa.

Six Co/Cu segmented samples were fabricated, with cobalt being deposited for 20 and 80 seconds, and copper for 290, 580, and 870 seconds, plus sample C represented in table 4.1, corresponds to non-segmented Co nanowires deposited for 1 hour and 45 minutes.

Figures 4.1 and 4.2 show the current response to the electrodeposition process for samples A1 and B1 respectively. It is clear that during the deposition of the cobalt segments, the current did not reach a steady state after the sudden potential step.
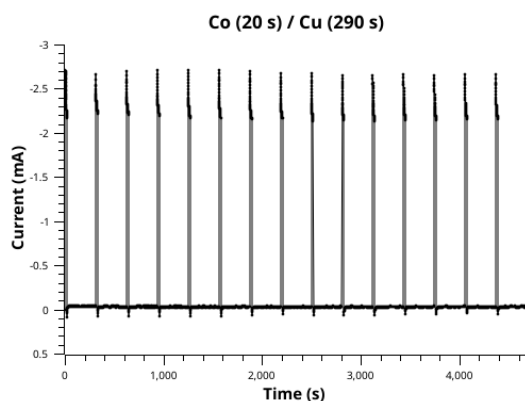
FIGURE 4.1: Current response of the electrodeposition process for sample A1.
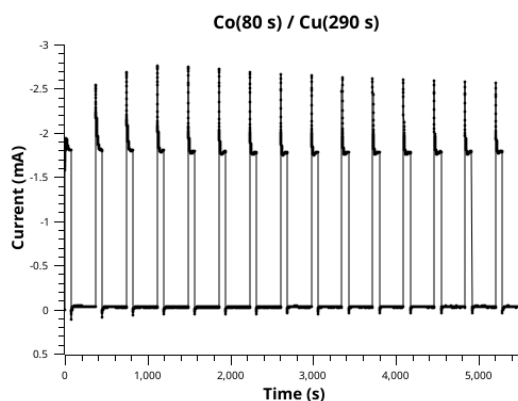
FIGURE 4.2: Current response of the electrodeposition process for sample B1.

Figure 4.3 shows the current of the electrodeposition process of a cobalt segment of a Co/Cu sample with longer cobalt segments.

The electric potential is initially at -0,6 V, with copper being deposited. At $t = 0$ the potential is switched to -1 V and remains constant for 40 seconds when it returns to -0,6 V. A dynamic phase of the electrodeposition process occurs after the potential step, before

FIGURE 4.3: Electrodeposition of a Co segment.

the system reaches a steady state where the current slightly decreases with time. The same behaviour is observed in the electrodeposition curves of samples A and B (figures 4.1 and 4.2), however the Co deposition ends at different stages of the dynamic phase, which are marked by the blue lines in figure 4.3.

This change in the current intensity can be solely due to the chemical reactions occurring in the electrolyte before it reaches equilibrium, without affecting the nanowires growth. However, a possibility must be considered, that the structural and chemical composition of the wires being deposited are affected during this initial phase of the electrodeposition, leading to non-homogeneous nanowires. It is therefore possible, that samples A and B, whose segments were deposited for 20 and 80 seconds respectively, have different structural and chemical compositions, despite having been fabricated with the same electrolyte and under the same conditions.

Similar conclusions were previously reached for pulsed electrodeposition of non-segmented Co nanowires and for segmented Co/Cu nanowires employing a dual-bath method in [69, 70], which proposes the control of the mangetic anisotropy by the electrodeposition time, not letting the deposition reach an equilibrium state.

With this possibility under consideration, and in order to ensure homogeneity in most of the wire length, an electrolyte with less Co concentration could be used, at the cost of copper contamination, so that the possible defects occuring during the dynamic phase of the electrodeposition are but an interface occurrence.

4.2 Scanning electron microscopy

The two proton difference between cobalt and copper elements results is little contrast on SEM visualization. Particularly considering the signal from the nanowires behind the cross-section, whose segments are not necessarily aligned. Backscattered electrons are emitted from depths of the order of the micrometre, while the alumina templates inter-pore distance is of 105 nm. This results in considerable noise from the wires deeper within the sample.

The reported Co/Cu selective etchants were unsuccessful in selectively removing the segments [71–73].

Figures 4.4 and 4.5 show the cross-section view of Co/Cu segmented wires, where segments were removed, purely by chance, when breaking the sample to expose the cross-section. This, however, is a rather rare and uncontrolled event and only occurs in particular areas of the cross-section.

The solution found was to disperse the wires in a silicon wafer, by removing the sputtered gold contact with an aqueous solution of 5 % I_2 and 10 % KI. and dissolving the alumina templates in a solution of 0,4 M phosphoric acid (H_2PO_4) and 0,2 M chromic acid (H_2CrO_4) at 40 º Celsius, with occasional agitation. The wires are then captured with a permanent magnet and washed with ethanol.

Figures 4.6 and 4.7 are examples of the images acquired in SEM. The segments are clearly observed in these images, with the copper segments much brighter than the cobalt ones.

The bright top segment in the nanowires of figure 4.7 and at the bottom in figure 4.4 corresponds to the gold electrodeposited in order to improve the electric contact of the sputtered layer, which is not removed by the chemical etching.
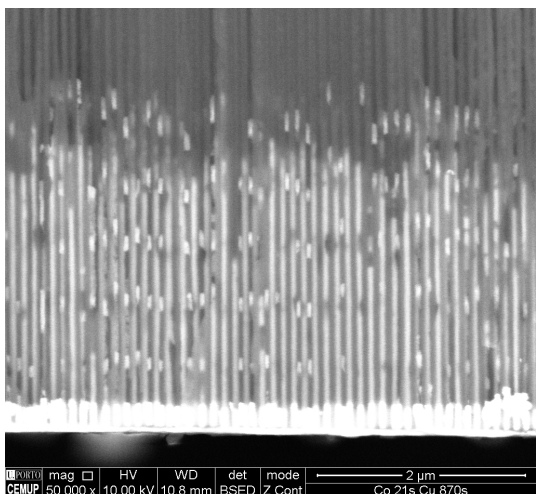
FIGURE 4.4: Copper segments in a cross-section view. The cobalt segments were removed.
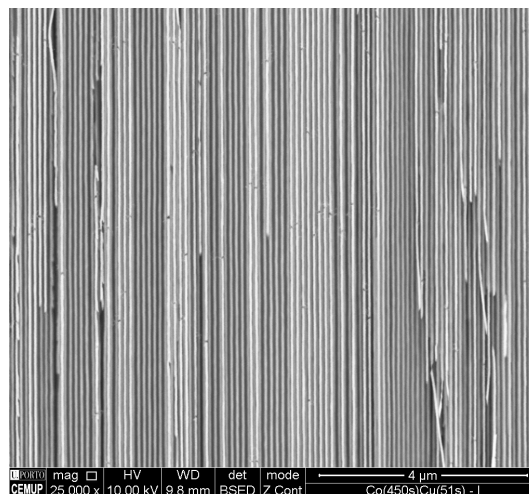
FIGURE 4.5: Cobalt segments in a cross-section view. The copper segments were removed.
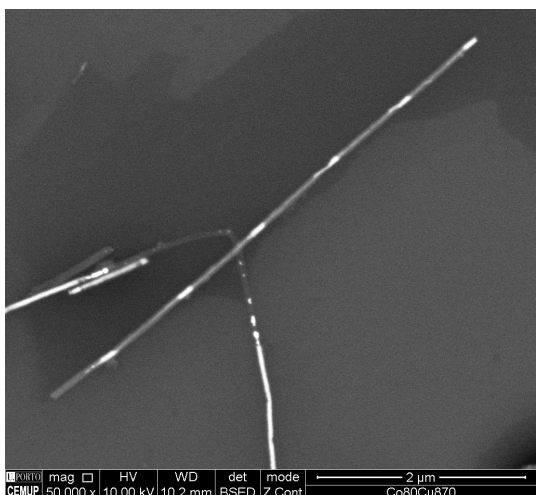
FIGURE 4.6: Co/Cu segmented nanowire. The bright segments correspond to copper while the darker ones correspond to cobalt.
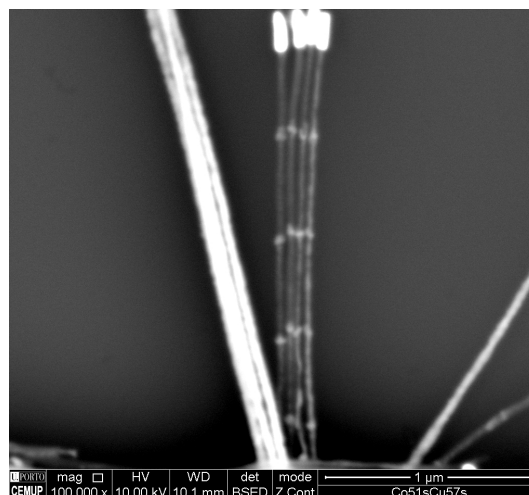
FIGURE 4.7: Co/Cu segmented nanowires. The brightest segments at the top end of the wires correspond to the gold contact.

EDS shows a significant increase in oxygen when probing the cobalt segments, indicating a rather fast oxidation cobalt nanowires. Oxidation results in a decrease in density which would further improve the visualization contrast. Another possibility for the presence of oxygen in the EDS spectrum is the formation of a hydroxide during the electrodeposition of cobalt [74].

This improved contrast permitted the measurement of the nanowires segments, tabeled in table 4.1.

An exact control of the segments length is hard to achieve. Samples A3 and B2 have abnormal Co segments. This could simply be a statistical error of the specific nanowires

Sample	Deposition time	Segment length
A1	Co(20 s) / Cu(290 s)	Co (250 nm ± 30 nm) / Cu (80 nm ± 10 nm)
A2	Co(20 s) / Cu(580 s)	Co (250 nm ± 30 nm) / Cu (150 nm ± 10 nm)
A3	Co(20 s) / Cu(870 s)	Co (400 nm ± 50 nm) / Cu (180 nm ± 10 nm)
B1	Co(80 s) / Cu(290 s)	Co (1000 nm ± 100 nm) / Cu (80 nm ± 10 nm)
B2	Co(80 s) / Cu(580 s)	Co (800 nm ± 100 nm) / Cu (120 nm ± 10 nm)
B3	Co(80 s) / Cu(870 s)	Co (1000 nm ± 100 nm) / Cu (150 nm ± 10 nm)
C	Co(1 h 45 min)	Co(60 μm ± 5 μm)

TABLE 4.1: Deposition times and segment lengths of the Co/Cu samples.

captured by SEM imaging, or it could be due to the position of the reference electrode, which is manually placed, and therefore there is a significant error in its distance to the working electrode.

4.3   Structural characterization

$\theta/2\theta$ XRD measurements were performed with Bragg-Brentano geometry. All segmented samples were measured with the bottom (Au contact) up, while the non-segmented sample C was measured with the top up.

Cobalt is known to have both a hexagonal closed packed (hcp), and face-centred cubic (fcc) structure. Fcc cobalt has four magnetocrystalline easy axes (c-axis), along each of the cubic cells diagonals, and its contribution to the magnetic anisotropy can usually be neglected, while the hcp structure has the [001] direction as the single c-axis.

In figure 4.8, a schematic of the magnetocrystalline and shape anisotropies, for the detected XRD peaks, is shown. The contribution of shape to the magnetic anisotropy is always along the wires axis. The (002) texture, which corresponds to the [001] direction of
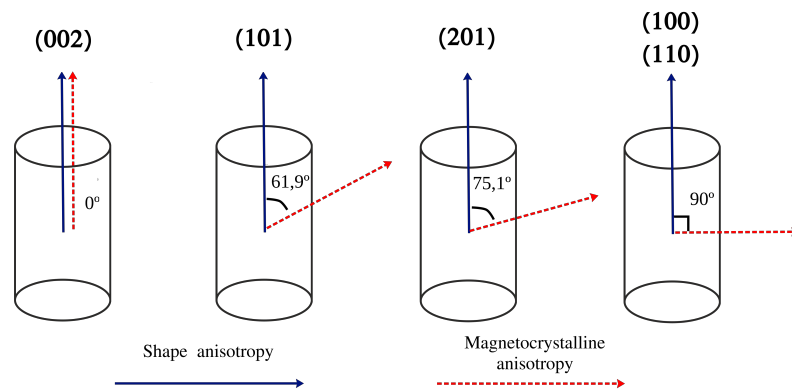
FIGURE 4.8: Schematic of shape and magneticrystalline anisotropy in hcp Co nanowires.

the hexagonal cell, has the c-axis aligned with the wires axis, adding to shape anisotropy. In the (100) and (110) textures, the c-axis is perpendicular to the wire axis, while the (101) and (201) textures, the c-axis is at an angle with the wire axis of 61,9° and 75,1° respectively, leading to competing shape a magnetocrystalline anisotropy.
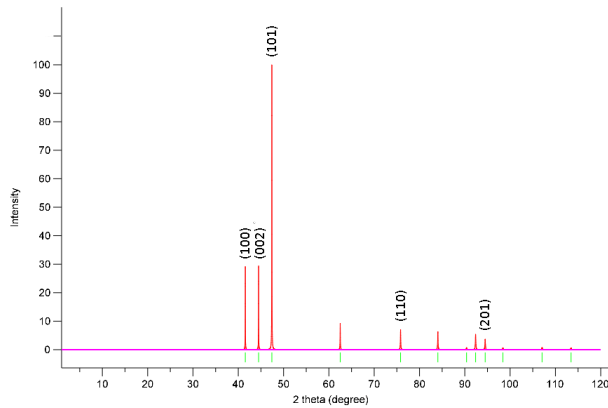
FIGURE 4.9: Relative intensities of hcp cobalt powder.

Figure 4.9 shows the X-ray diffraction pattern for hcp cobalt powder, in which all the crystallographic directions are equi-probable. It shows the relative intensity of the diffracted peaks, where (101) is by far the most intense, the (100) and (002) are of medium intensity. (110) has relatively low intensity while (201) has the lowest intensity of the peaks observed in the characterized samples (figures 4.10, 4.11 and 4.12).

In figures 4.10 and 4.11, Au and Cu is always fcc, while Co has a hcp structure by omission.

For samples B (figure 4.11), which have the longer cobalt segments, the relative intensities indicate a strong preferential direction in the (201) planes, consequentially putting the c-axis at an angle of 75,1° with the wires axis.

The (101) peak, which is the most diffractive family planes, has low intensity, indicating a very low (101) contribution to the overall crystallographic structure.
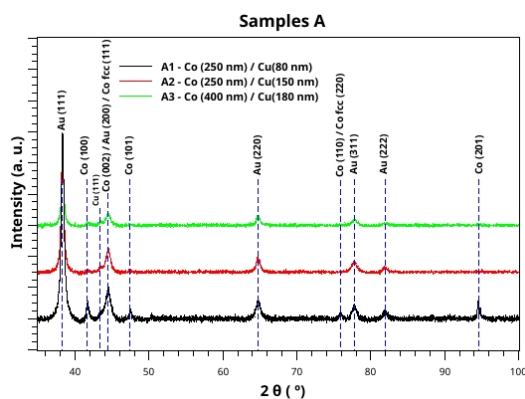
FIGURE 4.10: X-ray diffraction pattern for samples A.
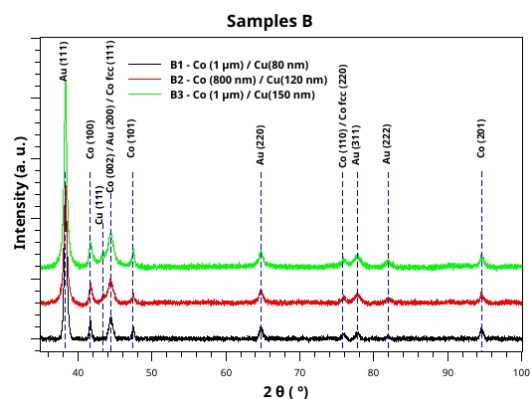
FIGURE 4.11: X-ray diffraction pattern for samples B.

The peak at $2\theta = 44,4^{o}$, visible at all segmented samples can be attributed to either gold, Co hcp and Co fcc. Comparison with a control sample with only the gold contact, sputtered and electrodeposited on the alumina template, indicates that most of this peak is due to gold, with the rest being either a hcp or fcc structure of cobalt. If it is due to fcc (111), its contribution to the magneticrystalline anisotropy would be negligible. On the other hand, if its due to hcp (002) crystallographic planes, its contribution would move the c-axis towards the wire axis in the [001] direction, adding to the shape anisotropy.

The gold contact is rather difficult to remove due to the Au electrodeposition process filling the bottom of the pores, forming a gold nanowire segment (figures 4.4 and 4.7). For further studies, nanowire fabrication should be performed at least with considerably lower Au electrodeposition time.

Finally, the second most significant contribution to the magnetocrystalline anisotropy are the hcp (100) and (110) planes, both of which put the c-axis perpendicular to the wire axis, resulting in competing shape and crystallographic anisotropies.

Samples A have less material deposited. With the exception of sample A1, hcp Co peaks (100) and (101), are almost unnoticeable. Again, the $2\theta = 44,4^{o}$ peak is mostly due to gold and the Co fcc (111) has a negligible contribution to anisotropy, while the hcp Co (002) peak would put the c-axis contribution in the wires axis direction. This indicates that, either the amount of cobalt deposited is not enough to be detected for the conditions in which the measurements were performed, or cobalt has a mostly amorphous structure in the first stages of electrodeposition.

Sample A1 Co(250 nm) / Cu(80 nm), has a similar crystallographic structure to samples B, where there is a significant perpendicular to wires contribution to the magnetocrystalline anisotropy.

By comparing samples A and B, in which the cobalt segments were deposited for 20 and 80 seconds respectively, it appears that the structural composition of the Co segments change with the electrodeposition time. It was previously seen that the electrodeposition process enters a new phase at around the first 20 seconds after the potential step. In fact, the cobalt segments of samples A were deposited for precisely the time when the electrodeposition enters a new phase. This can explain the fact that sample A1 Co(250 nm) / Cu(80 nm) has a similar crystallographic structure to samples B, and gives further indication of a structural change in the different phases of the electrodeposition process.

In references [69, 70], it was concluded that the initial non-equilibrium deposition corresponds to a nanowire growth in the fcc (111) orientation. In that study, however, a pulsed electrodeposition was performed, and either non-segmented wires were deposited, or segmented wires were deposited by two distinct electrolyte baths. This results in the initial potential step, before the deposition of cobalt being of -1 V, instead of -0,4 V. This potential step results in a different behaviour of the current response, as can be seen in the first Co segments of figures 4.1 and 4.2.

It is rather difficult to reach such conclusion with the results obtained in this work due to the superposition of the Au (200) from the electrical contact. Plus, the Co hcp (002) peak also superposes with fcc (111). In any case, the result is having the magnetic easy axis (EA) along the wire axis.

Figure 4.12 shows the diffraction pattern for sample C. A strong orientation of the (101) planes appears, with the (100) peak also visible. The (101)
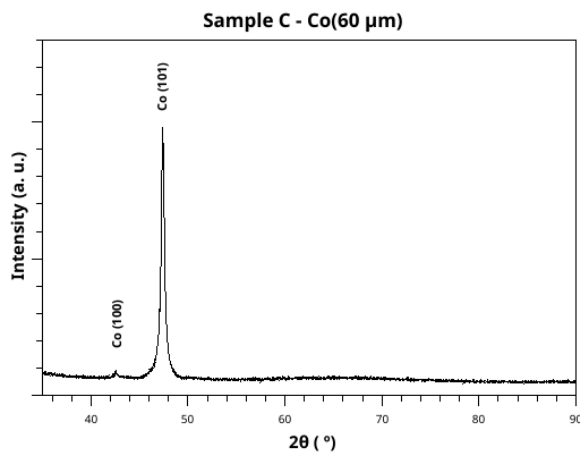
FIGURE 4.12: X-ray diffraction pattern for sample C.

plane orientation would put the c-axis at an angle of 61,9º with the wires axis and therefore compete with shape anisotropy. It must be noted that the measurement was only performed up to $2\theta = 90º$. Therefore, the question emerges whether the wires keep a (201) preferential orientation, as in samples B, or at some point during the electrodeposition equilibrium phase, it changes to a (101) preferential orientation. This would be consistent with the results in reference [53], where it was shown that the a distinct crystallographic structure appears for electrodeposited Co nanowires of 3 and 30 micrometres.

4.4 Magnetic characterization

M(H) measurements were performed with a SQUID magnometer at room temperature. Figure 4.13 shows the magnetic hysteresis for all samples with the field applied parallel to the wire' long axis.
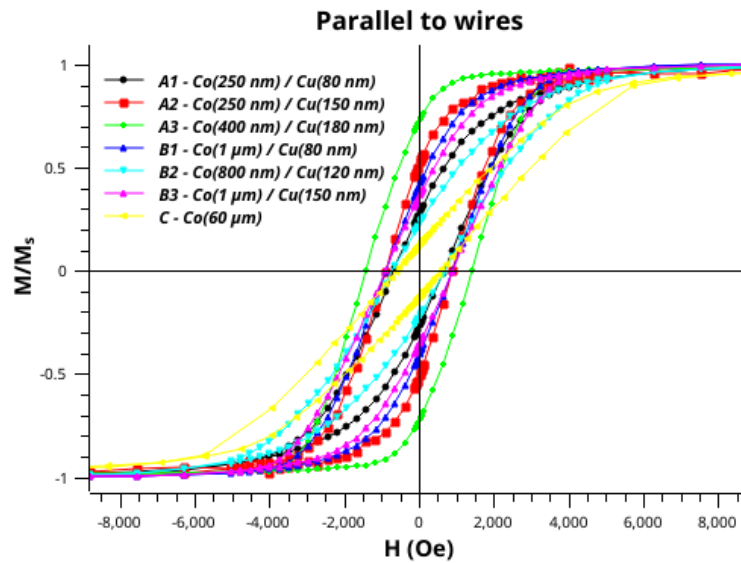
FIGURE 4.13: M(H) for field applied parallel to the wires.
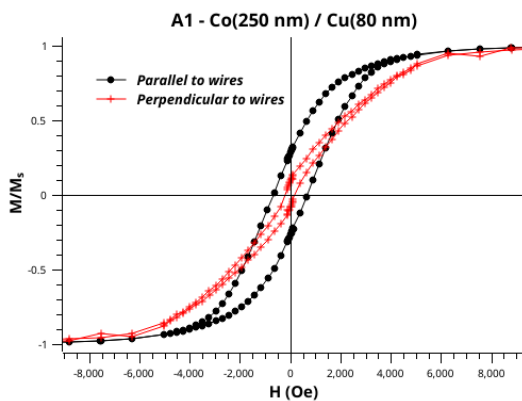
FIGURE 4.14: M(H) for sample A1 with the field applied parallel and perpendicularly to the wires.
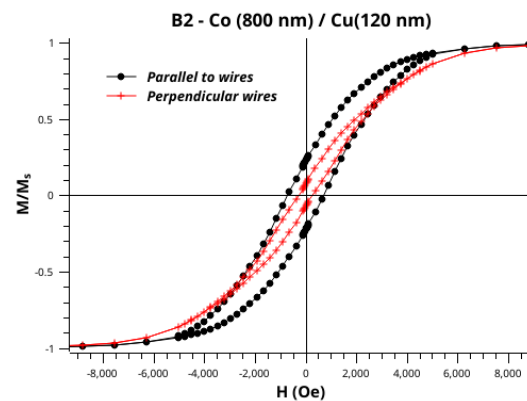
FIGURE 4.15: M(H) for sample B2 with the field applied parallel and perpendicularly to the wires.

Samples A2 and A3 exhibit the most squared hysteresis cycles. This signifies that they are the ones with magnetic EA closest to wires axis, even though the barely detected structure hcp (100) puts the c-axis perpendicular to the wires. It is then clear that the magnetic anisotropy for samples A2 and A3 results from shape and possibly from a contribution from the magnetocrystalline anisotropy of the hcp structure in the [001] direction.

Sample A3 Co(400 nm) / Cu(180 nm) has a considerable larger coercivity and remanence than sample A2 Co(250 nm) / Cu(150 nm). Since they have similar crystallographic structure, and the dipolar interactions between the Co segments, which are stronger for shorter Cu spacings, should have the opposite effect, this must be due to the longer Co segments of sample A3.

The shape of the Co segments cannot be the only contribution to magnetic anisotropy. Sample A1 - Co(250 nm) / Cu(80 nm), has the same Co segment length as sample A2 - Co(250 nm) / Cu(150 nm), and the dipolar interactions between the Co segments would put the magnetic EA of sample A1, closer to the wire axis due to shorter Cu spacings. Yet the opposite is observed. The magnetic behaviour of sample A1 can therefore only be explained by the crystalline structure, which is consistent with the XRD results in which a (201) preferential orientation is observed with a strong contribution from the (100) and (110) orientations, leading to competing shape and magnetocrystalline anisotropy. The same applies to samples B, which have considerably longer Co segments, and exhibit less hysteresis than samples A2 and A3. It is then clear that structure plays an important role in the magnetic anisotropy after the first stages of electrodeposition.

All B samples have similar crystallographic structure. The low hysteresis of sample B2 - Co(800 nm) / Cu (120 nm) should be due to the lower aspect ratio of the cobalt segments. The greater hysteresis of sample B1 - Co(1000 μm) / Cu (80 nm) relatively to B3 - Co(1000 μm) / Cu (150 nm) can be attributed to the stronger dipolar interactions between the cobalt segments, due to the shorter copper spacer.

Shape, however, is still the dominant factor for the segmented samples Of all the segmented samples, A1 and B2 are the ones with the least hysteretic behaviour. Figures 4.14 and 4.15 show greater hysteresis when the field is applied parallel to the wires axis for these samples and therefore, the mangnetic EA is closer to the wires axis than perpendicular to it.

The non-segmented sample (C - Co (60 μm)) is the one with the least hysteretic behaviour. Figure 4.16 shows the M(H) of sample C with the field applied parallel and perpendicular to the wires. The hysteresis loops show no apparent magnetic anisotropy, meaning that the EA is close to a 45 º angle with the wires axis.
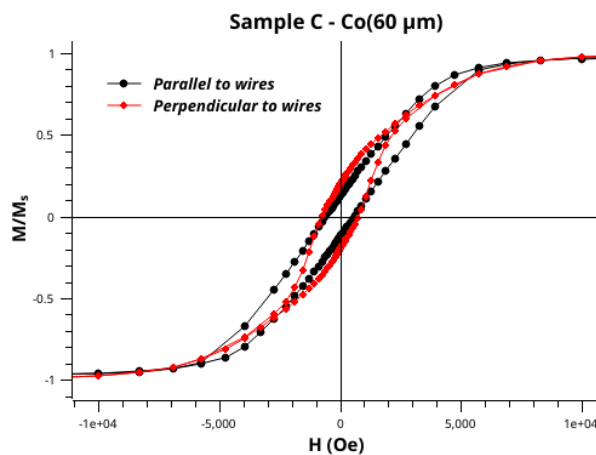

FIGURE 4.16: Hysteresis loops of sample C with the field applied parallel and perpendicular to the wires axis.

4.5   Co/Au nanowires

The difficulty in differentiate the cobalt and copper segments in electron microscopy motivated the fabrication of Co nanowires with constrictions of an alternative element. Since the deposition of gold was already being performed with the commercial gold-plating solution, Co/Au segmented nanowires were fabricated. For this material combination, a dual-bath method is necessary. For the deposition of Co, the same solution as the previous wires was used minus the Cu ions. For the Au deposition, the Orosene solution was used, also at -1 V.

Three samples were fabricated with 10 Co/Au segments. The Co segments were deposited for 200 seconds and gold was deposited for 20, 40 and 60 seconds.

- Co (200 s) / Au (20 s)

- Co (200 s) / Au (40 s)

- Co (200 s) / Au (60 s)

It was already established that an exact control of the segments length is hard to achieve, and that different wires grow at slightly different rates, attributing an error to the nanowires length. However, the length of the segments within the same wire has consistently been constant. This is not observed on the Cu/Au wires. In figures 4.17 and 4.18, centred in a cobalt segment, it can be seen that the gold constrictions at the lower end of the image are significantly shorter than the ones at the top. This fact can be attributed to the manual placing of the reference electrode, which has to be placed each time the electrolyte is changed, and whose distance to the working electrode (sample) is not precisely controlled. It is also observed some defects on some wires where a Au segment is deposited almost immediately after the previous one, with very little cobalt in between them. It is possible that it is rather difficult to properly wash the sample at each bath switch, and that some of the previous electrolyte bath remains inside the pores. It is clear that the quality of these samples is considerably inferior to the Co/Cu nanowires fabricated employing the single-bath method.

The difference in segment length is even more evident in figure 4.19, where the wires have grown orders of magnitude shorter than the rest, likely due to some defects in the electrical contact or some obstruction in the pore that limits the diffusion of the electrolyte
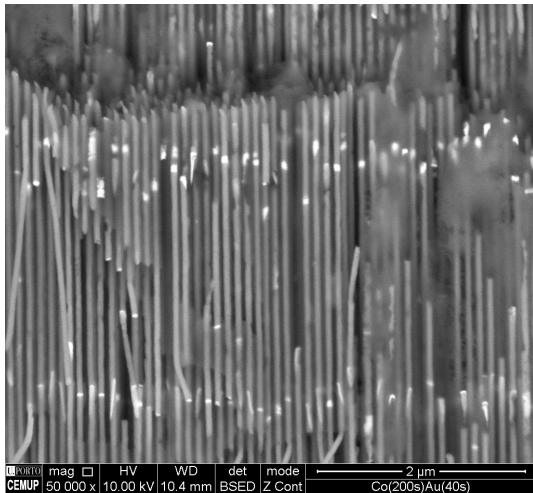
FIGURE 4.17: Co/Au nanowires, centred in a Co segment.
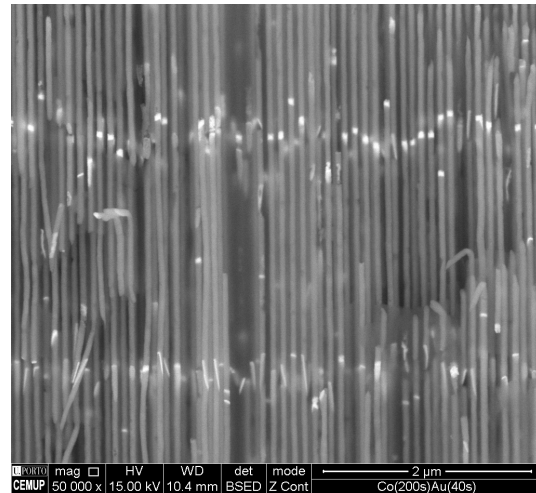
FIGURE 4.18: Co/Au nanowires, centred in a Co segment.
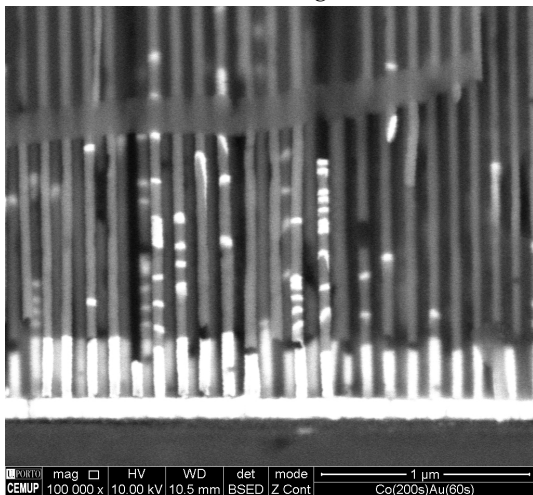
FIGURE 4.19: Nanowires bottom. Some wires are grown orders of magnitude shorter than the average.
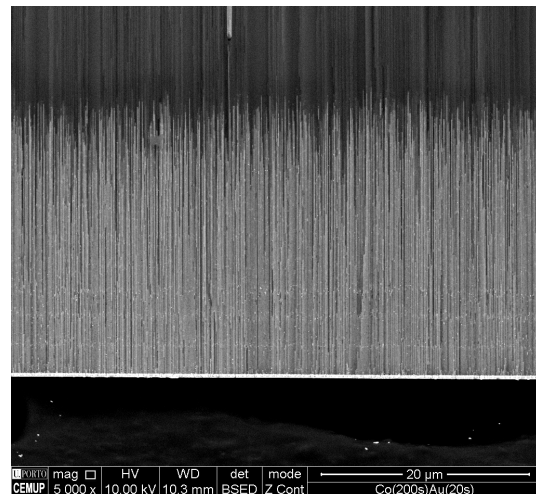
FIGURE 4.20: Overview of the whole length of the nanowires.

ions. Although it is possible that the formation of these nanowires, could have also occurred for the Co/Cu and Ni/Cu samples, the variation of segment length within the same wire is evident in these shorter wires.

Figure 4.19 shows a less zoomed image of a Co/Au sample, showing the whole length of the nanowires. Horizontal bright lines can be seen which correspond to the gold segments. The first two Au segments are clearly defined while the third is slightly less clear The remaining Au segments are rather hard to notice. This is the result of the multiplication of the error of segments length, as each segment is deposited.

This led to a difficulty in attributing a value to the segments length, and therefore the samples will be referred to by their deposition times.
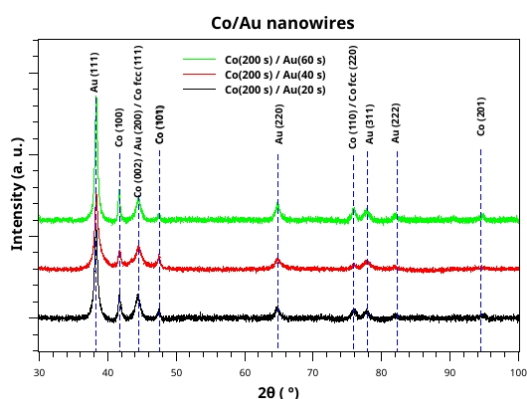
FIGURE 4.21: X-ray diffraction pattern for Co/Au nanowires.
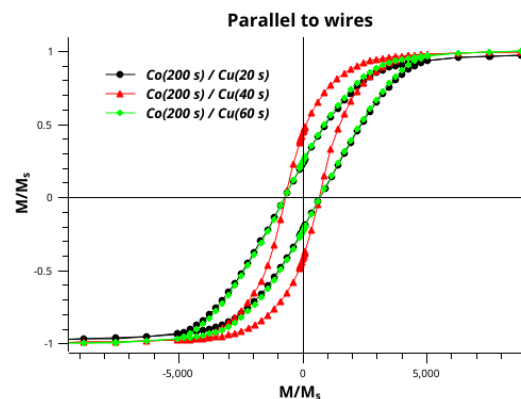
FIGURE 4.22: M(H) of the Co/Au samples with the field applied parallel to the wires.

Figure 4.21 shows the diffraction pattern of the Co/Au samples.

In the previous Co/Cu nanowires, preferential orientations were (201) and (101) for long non-segmented nanowires. In the Co/Au nanowires, the (201) samples were almost unnoticeable, however still relevant due to the low diffractiveness of these planes. Although the Co segments were deposited for considerably longer than the Co/Cu ones, the (101) contribution is very small, either because it did not have enough time to form, as in sample C, or the electrodeposition conditions do not favour such orientation. There is, however, a slight increase in the (100) peak, particularly in samples Co(200)Au(20s) and Co(200)Au(60s). The result of this difference can be seen in figure 4.22 where Co(200)Au(40s) has a more squared hysteresis loop.

The differences in the crystallographic growth of these samples can be attributed to several factors:

1. Different crystallographic structures can be grown, depending on the substrate. It is therefore possible that the cobalt segments grow with a distinct crystallographic structure when they are deposited on a Au segment rather than on a Cu segment.

2. The electrolyte used for the electrodeposition is different and therefore the reactions occuring are also different.

3. The absence of copper contamination in the deposited cobalt can affect its preferential crystallographic structure.

4. Finally, the postential step at the start of each Co segment deposition is of -1 V rather than -0,4 V. This can affect the initial dynamic phase of the electrodeposition.

Overall, the quality of the Co/Au samples is of inferior when compared to the Co/Cu samples. The electrolyte solution had to be manually changed for each segment deposited which is a tedious and time consuming process that greatly increases the probability of human error. It is therefore not viable for any industrial application in the manner in which it was performed. This calls for the development of an automated bath-switching electrodeposition cell and one that fixes the reference electrode at a determined position.

4.6   Conclusions

Cobalt nanowire arrays with gold and copper constraints were fabricated by DC electrodeposition on nanoporous alumina templates. A precise control of the Co and Cu segments length is hard to achieve with the methods employed.

The samples were characterized by SEM, EDS, XRD and SQUID. Copper contamination in the cobalt segments is not detected by EDS. The dispersion of segmented nanowires with small atomic number difference between segments in a silicon wafer improves the contrast for electron microscopy visualization. This is partly due to the improved microscopy conditions, and partly due to the decreasing density of the Co segments by oxidation.

The magnetic anisotropy of Co wires is highly dependent on the crystalline structure. Different phases of the electrodeposition of Co segments can be identified. There are indications of a change in preferential crystallographic structure with the different phases. This could provide a path to controlling the magnetic anisotropy of multi-segmented Co nanowires. fabricatend by DC electrodeposition, employing the single-bath method. However, a more conclusive and systematic study is required.

An alternative solution to the gold contact electrodeposition should be explored for further studies of Co nanowire fabrication, so as to not have the superposing Au peaks in the XRD pattern of the samples, either by reducing the time of Au electrodeposition, or eliminating it altogether. The sputtered gold layer could also be substituted by copper.

For longer, non-segmented nanowires (sample C), and for the electrodeposition conditions used, a strong (101) crystallographic orientation emerges. However, it is not clear if this is a preferential growth direction or a (201) preferential orientation is kept. In any case, this results in the magnetocrystalline anisotropy competing with shape, leading to a magnetic EA close to a 45° angle with the wires axis.

The Co/Au samples, electrodeposited using a double-bath method, were found to be of inferior quality when compared to the Co/Cu samples. The repetitive and time consuming process of switching the electrolyte baths greatly increases the probability of human error. The development of an automated bath-switching electrodeposition cell is called for.

Chapter 5

Conclusions and Ongoing Work

Micromagnetic simulations were performed in order to study the magnetic reversal modes, and the DW nucleation in non-magnetic spacings.

The magnetization reversal process was found to occur in three distinct modes, either by nucleation and propagation of a TDW, VDW, or by coherent rotation, where all magnetic moments revert simultaneously. The mode in which the wires magnetization revert depends essentially on the nanowires diameter. For aspect ratios larger than 5, nickel nanowires can be considered as if they were infinite. Domain wall nucleation occurs at the nanowires ends and for spacings longer than 20 nm.

A micromagnetic study on the dynamics of the magnetization reversal process is required, particularly on the movement of DWs in nanowires with non-magnetic constraints, both by pulses of magnetic field and by spin-polarized current.

Simulation of cobalt nanowires should also be performed in the near future to study the effect of a large magnetocrystalline anisotropy in the dynamics of the magnetic behaviour of nanowires. The simulation of a polycrystalline structure is rather tricky. The crystallite grain structure is modelled by the Voronoi tessellation which is built into the Mumax3 code. To each crystallite is assigned a random c-axis considering the experimental results acquired by the structural characterization, such as the preferential orientations and the crystallite size. For example, a cobalt nanowire has an hcp (101) polycrystalline structure, the crystallite c-axis vectors are randomly distributed on the surface of a cone of 61,9 º with respect to the wire axis. The same simulation can therefore have slightly different results as the grain distributions differ from simulation to simulation. Therefore, each simulation should be ran several times in order to determine the variations of the magnetic behaviour due to the randomness of the grain distribution.

Arrays of nickel and cobalt nanowires with chemical constraints were fabricated by electrodeposition on nanoporous alumina templates. The samples were characterized by SEM, EDS, XRD and SQUID.

It was found that the precise control of the nanowires segments is difficult to achieve by electrodeposition. A dynamic behaviour occurs when the electrodeposition potential is varied for the deposition of each segment. Distinct phases are identified within this dynamic behaviour. There are indications of crystallographic structural changes in the nanowire growth with respect to these phases. This could provide a new method of controlling the magnetic anisotropy of multi-segmented Co nanowires. The controlled electrodeposition of non-magnetic Ni-hcp structure could provide a way of fabricating nickel nanowires with structural constraints for the control of magnetic domain walls for spintronic devices. However, a more conclusive and systematic study is required.

The small atomic number between Ni, Co and Cu elements results in negligible contrast between the nanowires segments. The solution employed for the Ni/Cu samples was to selectively etch the copper segments. For the Co/Cu samples, no selective etchant was found, however the dispersion of the nanowires onto a silicon wafer improves the contrast for electron microscopy visualization. This is, in part, due to the improved microscopy conditions, and possibly due to the decreasing density of the Co segments by oxidation.

The oxidation of cobalt nanowires gives prospects for some interesting results. One of the cobalt (CoO) is anti-ferromagnetic. As an oxide layer forms around the nanowire, an exchange bias effect should emerge. This effect as been previously reported for cobalt nanotubes in an alumina membrane where the inner surface of the tubes is exposed to the air, forming the antiferromagnetic layer [75].

Non-segmented nanowires (of sample C) were dispersed using the same method as in chapter 4. The nanowires were orientated by placing a drop of ethanol, with the wires dispersed in, between two permanent magnets, and letting the ethanol evaporate. The wires were then left to oxidize still between the magnets so as to force the direction of the antiferromagnetic axis.

M(H) measurements are being performed with a SQUID at temperatures from 300 K to 5 K so as to determine the wires Neél temperature (which is 291K for bulk CoO), and to observe the oxidation process. About three and a half months after the nanowires were dispersed and left to oxidize, an exchange bias effect was observed at all temperatures
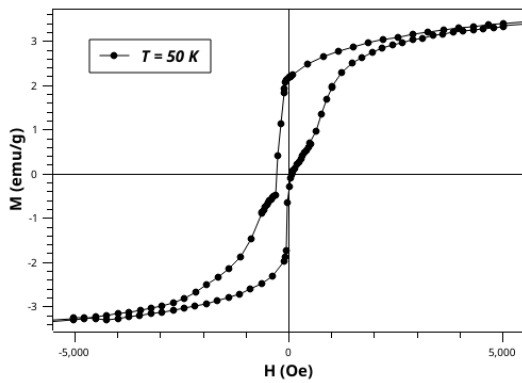
FIGURE 5.1: Exchange biased hysteresis loop at 50K.
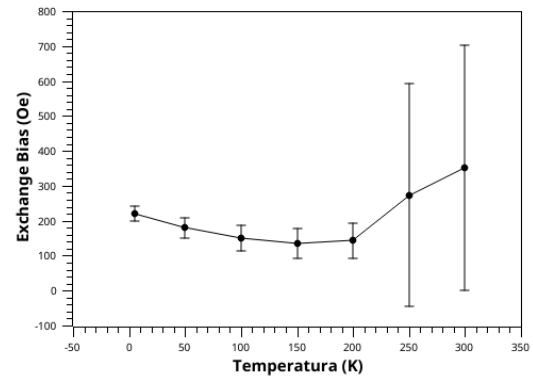
FIGURE 5.2: Exchange bias effect versus the temperature.

measured, indicating an increase of the Néel temperature above 300K for this nanoscaled material.

Figure 5.1 shows an example of the exchange biased hysteresis loop, at 50 K. The hysteresis loops exhibit similar behaviour for all temperatures measured. However, the measurement needed to be rectified after the first two measurements (300K and 250K) in order to obtain more points near te coercive field. This resulted in a large error for temperatures 250K and 300K in plotting the exchange bias in figure 5.2.

These results call for the repetition of the measurements with an increased number of points near the coercive field in order to reduce the error of the exchange bias, and at higher temperatures in order to determine the Néel temperature.

From the hysteresis loops, it is clear that the magnetization reversal process is more complex than conventional magnetic nanowires. The determination of the reversal modes can be done with the assistance of micromagnetic simulations. An interesting possibility that emerges is the fabrication of cobalt nanowires with oxidized segments, possibly serving as DW pinning sites.

Bibliography

[1] C. T. de Sousa, *Development of Nanoporous Alumina Templates for Biotechnological Applications*, Ph.D. thesis, Faculdade de Ciências da Universidade do Porto (2011).

[2] A. O. A. da Silva Apolinário, *Nanostructured Photoanodes for Solar Cells*, Ph.D. thesis, Faculdade de Ciências da Universidade do Porto (2015).

[3] G. E. Moore *et al.*, "Cramming more components onto integrated circuits," (1965).

[4] E. Grochowski and R. D. Halem, *Technological impact of magnetic hard disk drives on storage systems*, IBM Systems Journal **42**, 338 (2003).

[5] G. Moore, "Gordon moore: The man whose name means progress, the visionary engineer reflects on 50 years of moore's law," IEEE Spectrum: Special Report: 50 Years of Moore's Law (Interview). Interviewed by Rachel Courtland (March 30, 2015), https://spectrum.ieee.org/computing/hardware/gordon-moore-the-man-whose-name-means-progress (September, 2019).

[6] W. H. Meiklejohn and C. P. Bean, *New magnetic anisotropy*, Physical review **102**, 1413 (1956).

[7] W. H. Meiklejohn and C. P. Bean, *New magnetic anisotropy*, Physical Review **105**, 904 (1957).

[8] A. Berkowitz and K. Takano, *Exchange anisotropy—a review*, Journal of Magnetism and Magnetic materials **200**, 552 (1999).

[9] G. S. Abo, Y.-K. Hong, J. Park, J. Lee, W. Lee, and B.-C. Choi, *Definition of magnetic exchange length*, IEEE Transactions on Magnetics **49**, 4937 (2013).

[10] M. N. Baibich, J. M. Broto, A. Fert, F. N. Van Dau, *et al.*, *Giant magnetoresistance of (001) Fe/(001) Cr magnetic superlattices*, Physical review letters **61**, 2472 (1988).

[11] G. Binasch, P. Grünberg, F. Saurenbach, and W. Zinn, *Enhanced magnetoresistance in layered magnetic structures with antiferromagnetic interlayer exchange*, Physical review B **39**, 4828 (1989).

[12] "https://commons.wikimedia.org/," (September, 2019).

[13] W. Butler, X.-G. Zhang, D. Nicholson, and J. MacLaren, *Spin-dependent scattering and giant magnetoresistance*, Journal of magnetism and magnetic materials **151**, 354 (1995).

[14] B. Dieny, V. Speriosu, B. Gurney, S. Parkin, *et al.*, *Spin-valve effect in soft ferromagnetic sandwiches*, Journal of Magnetism and Magnetic Materials **93**, 101 (1991).

[15] B. Dieny, V. S. Speriosu, S. S. Parkin, B. A. Gurney, D. R. Wilhoit, and D. Mauri, *Giant magnetoresistive in soft ferromagnetic multilayers*, Physical Review B **43**, 1297 (1991).

[16] S. X. Wang and G. Li, *Advances in giant magnetoresistance biosensors with magnetic nanoparticle tags: Review and outlook*, IEEE transactions on Magnetics **44**, 1687 (2008).

[17] "https://www.hindawi.com/journals/acisc/2013/426962/fig12/," (September, 2019).

[18] S. Bhatti, R. Sbiaa, A. Hirohata, H. Ohno, S. Fukami, and S. Piramanayagam, *Spintronics based random access memory: a review*, Materials Today **20**, 530 (2017).

[19] R. L. Comstock, *Introduction to magnetism and magnetic recording* (Wiley, 1999).

[20] S. Parkin, K. Roche, M. Samant, P. Rice, *et al.*, *Exchange-biased magnetic tunnel junctions and application to nonvolatile magnetic random access memory*, Journal of Applied Physics **85**, 5828 (1999).

[21] D. C. Ralph and M. D. Stiles, *Spin transfer torques*, Journal of Magnetism and Magnetic Materials **320**, 1190 (2008).

[22] L. Berger, *Low-field magnetoresistance and domain drag in ferromagnets*, Journal of Applied Physics **49**, 2156 (1978).

[23] P. Freitas and L. Berger, *Observation of s-d exchange force between domain walls and electric current in very thin Permalloy films*, Journal of Applied Physics **57**, 1266 (1985).

[24] C.-Y. Hung and L. Berger, *Exchange forces between domain wall and electric current in permalloy films of variable thickness*, Journal of applied physics **63**, 4276 (1988).

[25] J. C. Slonczewski, *Current-driven excitation of magnetic multilayers*, Journal of Magnetism and Magnetic Materials **159**, L1 (1996).

[26] L. Berger, *Emission of spin waves by a magnetic multilayer traversed by a current*, Phys. Rev. B **54**, 9353 (1996).

[27] D. Apalkov, A. Khvalkovskiy, S. Watts, V. Nikitin, *et al.*, *Spin-transfer torque magnetic random access memory (STT-MRAM)*, ACM Journal on Emerging Technologies in Computing Systems (JETC) **9**, 13 (2013).

[28] E. Chen, D. Apalkov, Z. Diao, A. Driskill-Smith, *et al.*, *Advances and future prospects of spin-transfer torque random access memory*, IEEE Transactions on Magnetics **46**, 1873 (2010).

[29] R. Hertel, *Computational micromagnetism of magnetization processes in nickel nanowires*, Journal of Magnetism and Magnetic Materials **249**, 251 (2002).

[30] R. Hertel and J. Kirschner, *Magnetization reversal dynamics in nickel nanowires*, Physica B: Condensed Matter **343**, 206 (2004).

[31] M. Kläuia, H. Ehrke, and U. Rüdiger, *Direct observation of domain-wall pinning at nanoscale constrictions*, Applied Physics Letters **87** (2005).

[32] J. A. Fernandez-Roldan, R. P. del Real, C. Bran, M. Vazquez, and O. Chubykalo-Fesenko, *Magnetization pinning in modulated nanowires: From topological protection to the "corkscrew" mechanism*, Nanoscale **10**, 5923 (2018).

[33] D. Castilla, M. Maicas, J. Prieto, and M. Proenca, *Depinning process of magnetic domain walls in cylindrical nanowires with a chemical constraint*, Journal of Physics D: Applied Physics **50**, 105001 (2017).

[34] S. S. Parkin, M. Hayashi, and L. Thomas, *Magnetic domain-wall racetrack memory*, Science **320**, 190 (2008).

[35] S. Parkin and S.-H. Yang, *Memory on the racetrack*, Nature nanotechnology **10**, 195 (2015).

[36] M. de Jesus Paiva proença, *Magnetism at the Nanoscale: Nanoparticles, Nanowires, Nanotubes and their Ordered Arrays*, Ph.D. thesis, Faculdade de Ciências da Universidade do Porto (2012).

[37] A. Fernández-Pacheco, R. Streubel, O. Fruchart, R. Hertel, P. Fischer, and R. P. Cowburn, *Three-dimensional nanomagnetism*, Nature Communications **8**, 15756 (2017).

[38] A. Vansteenkiste, J. Leliaert, M. Dvornik, M. Helsen, F. Garcia-Sanchez, and B. Van Waeyenberge, *The design and verification of MuMax3*, AIP advances **4**, 107133 (2014).

[39] Y. P. Ivanov, M. Vázquez, and O. Chubykalo-Fesenko, *Magnetic reversal modes in cylindrical nanowires*, Journal of Physics D: Applied Physics **46**, 485001 (2013).

[40] H. Long, E. Ong, T. Liu, H. Li, *et al.*, *Micromagnetic simulations of magnetic nanowires with constrictions by FIB*, Journal of Magnetism and Magnetic Materials **303**, e299 (2006).

[41] W. Li, J. Zhang, T. Shen, G. A. Jones, and P. J. Grundy, *Magnetic nanowires fabricated by anodic aluminum oxide template—a brief review*, Science China physics, mechanics and astronomy **54**, 1181 (2011).

[42] G. Yang, B. Wang, K. Tawfiq, H. Wei, S. Zhou, and G. Chen, *Electropolishing of surfaces: theory and applications*, Surface Engineering **33**, 149 (2017).

[43] G. Bengough and J. Stuart, *Improved process of protecting surfaces of aluminium of aluminium alloys*, UK patent **223** (1923).

[44] R. Furneaux, W. Rigby, and A. Davidson, *The formation of controlled-porosity membranes from anodically oxidized aluminium*, Nature **337**, 147 (1989).

[45] H. Masuda and K. Fukuda, *Ordered metal nanohole arrays made by a two-step replication of honeycomb structures of anodic alumina*, science **268**, 1466 (1995).

[46] W. Lee, *The anodization of aluminum for nanotechnology applications*, JOM **62**, 57 (2010).

[47] K. Nielsch, J. Choi, K. Schwirn, R. B. Wehrspohn, and U. Gösele, *Self-ordering regimes of porous alumina: the 10 porosity rule*, Nano letters **2**, 677 (2002).

[48] F. Li, L. Zhang, and R. M. Metzger, *On the growth of highly ordered pores in anodized aluminum oxide*, Chemistry of materials **10**, 2470 (1998).

[49] H. Masuda, H. Yamada, M. Satoh, H. Asoh, M. Nakao, and T. Tamamura, *Highly ordered nanochannel-array architecture in anodic alumina*, Applied Physics Letters **71**, 2770 (1997).

[50] "https://www.sciencedirect.com/topis/chemical-engineering/reactive-sputtering," (September, 2019).

[51] L. G. Vivas, *On the magnetic and structural properties of Co and Co-based nanowire arrays*, Ph.D. thesis, Departamento de Física de la Materia Condensada Universidad Autónoma de Madrid (2012).

[52] M. Wang, Z. Wu, H. Yang, and Y. Liu, *Growth Orientation Control of Co Nanowires Fabricated by Electrochemical Deposition Using Porous Alumina Templates*, Crystal Growth & Design **18**, 479 (2017).

[53] L. Vivas, J. Escrig, D. Trabada, G. Badini-Confalonieri, and M. Vázquez, *Magnetic anisotropy in ordered textured Co nanowires*, Applied Physics Letters **100**, 252405 (2012).

[54] M. Darques, A.-S. Bogaert, F. Elhoussine, S. Michotte, J. de la Torre Medina, A. Encinas, and L. Piraux, *Controlled growth of CoCu nanowires and application to multilayered CoCu/Cu nanowires with selected anisotropy*, Journal of Physics D: Applied Physics **39**, 5025 (2006).

[55] F. Tian, J. Zhu, D. Wei, and Y. Shen, *Magnetic field assisting DC electrodeposition: General methods for high-performance Ni nanowire array fabrication*, The Journal of Physical Chemistry B **109**, 14852 (2005).

[56] L. Goldman, C. Ross, W. Ohashi, D. Wu, and F. Spaepen, *New dual-bath technique for electrodeposition of short repeat length multilayers*, Applied physics letters **55**, 2182 (1989).

[57] C. Ross, L. Goldman, and F. Spaepen, *An Electrodeposition Technique for Producing Multilayers of Nickel-Phosphorus and Other Alloys*, Journal of The Electrochemical Society **140**, 91 (1993).

[58] "sites.ualberta.ca," (September, 2019).

[59] C. Sá, "Caracterização morfológica, microestrutural e microanalítica de materiais por: microscopia electrónica de varrimento - SEM e microanálise por raios X - EPMA: EDS/WDS," Centro de Materiais da Universidade do Porto (CEMUP), (2006).

[60] "http://pd.chem.ucl.ac.uk/ pdnn/inst1/ optics1.htm," (September, 2019).

[61] "https://ywcmatsci.yale.edu/principle-0," (September, 2019).

[62] M. P. Proenca, C. T. Sousa, J. Ventura, J. P. Araujo, J. Escrig, and M. Vazquez, in *Spin*, Vol. 2 (World Scientific, 2012) p. 1250014.

[63] K.-M. Yin and B.-T. Lin, *Effects of boric acid on the electrodeposition of iron, nickel and iron-nickel*, Surface and Coatings Technology **78**, 205 (1996).

[64] J. Higuchi, M. Ohtake, Y. Sato, and M. Futamoto, in *Journal of Physics: Conference Series*, Vol. 303 (IOP Publishing, 2011) p. 012053.

[65] Z. Cheng, J. Zhu, and Z. Tang, *Magnetism of hexagonal closed-packed Ni nanowires from ab initio calculations*, Journal of Applied Physics **105**, 103906 (2009).

[66] C. Chinnasamy, B. Jeyadevan, K. Shinoda, K. Tohji, A. Narayanasamy, K. Sato, and S. Hisano, *Synthesis and magnetic properties of face-centered-cubic and hexagonal-close-packed Ni nanoparticles through polyol process*, Journal of applied physics **97**, 10J309 (2005).

[67] F. Tian, J. Zhu, and D. Wei, *Phase transition and magnetism of Ni nanowire arrays*, The Journal of Physical Chemistry C **111**, 6994 (2007).

[68] F. Zighem, T. Maurer, F. Ott, and G. Chaboussant, *Dipolar interactions in arrays of ferromagnetic nanowires: A micromagnetic study*, Journal of Applied Physics **109**, 013910 (2011).

[69] K. Pirota and M. Vazquez, *Arrays of Electroplated Multilayered Co/Cu Nanowires with controlled Magnetic Anisotropy*, Advanced Engineering Materials **7** (2005).

[70] K. Pirota, F. Béron, D. Zanchet, T. Rocha, *et al.*, *Magnetic and structural properties of fcc/hcp bi crystalline multilayer Co nanowire arrays prepared by controlled electroplating*, Journal of Applied Physics **109** (2011).

[71] J. Kelly, P. Bradley, and D. Landolt, *Additive Effects during Pulsed Deposition of Cu-Co Nanostructures*, Journal of The Electrochemical Society **147** (2000).

[72] J. Kelly, M. Cantoni, and D. Landolt, *Three-Dimensional Structuring of Electrodeposited Cu-Co Multilayer Alloys*, Journal of The Electrochemical Society **148** (2001).

[73] E. Stupnisek-Lisac, M. Karsulin, and H. Takenouti, in *Passivity of metals and semiconductors* (Elsevier, 1983) pp. 327–334.

[74] J. Santos, F. Trivinho-Strixino, and E. Pereira, *Investigation of $Co(OH)_2$ formation during cobalt electrodeposition using a chemometric procedure*, Surface and Coatings Technology **205** (2010).

[75] M. Proença, J. Ventura, C. Sousa, M. Vazquez, and J. Araujo, *Exchange bias, training effect, and bimodal distribution of blocking temperatures in electrodeposited core-shell nanotubes*, PHYSICAL REVIEW B **87** (2013).